

## Two-dimensional simulations of large-scale violent breaking wave impacts on a flexible wall

Zhengyu Hu, Yuzhu Li\*

National University of Singapore, Department of Civil and Environmental Engineering, Singapore

### ARTICLE INFO

**Keywords:**

Fully-coupled hydroelasticity  
Breaking waves  
Elastic wall  
Air entrapment  
OpenFOAM

### ABSTRACT

The impacts of four distinctive types of violent breaking waves on a flexible wall at a large scale are investigated using a fully-coupled computational fluid dynamics (CFD) and computational solid mechanics (CSM) model in the finite-volume framework, in which the CFD model simulates the incompressible two-phase (water-air) flow, and the CSM model considers a Neo-Hookean solid. The model is well validated against two experiments of the breaking wave impact on a rigid wall and the dam-break impact on an elastic wall. We then apply this model to study the interaction between the breaking waves and an elastic wall. Four types of breaking wave impact in terms of the *slightly-breaking*, *low-aeration*, *high-aeration*, and *broken-wave* impacts are considered and Cauchy number of the flexible wall ranges from 0.72 to 1.30. Compared with the rigid wall, it is found that the profile of peak pressure on the flexible wall shifts slightly upward. The impact force, impact duration, and impact impulse are affected (not necessarily reduced) by the structural deformation in progressive waves. The von Mises stress in the wall shows that the structural integrity of rigid and flexible walls is susceptible to the impact and maximum quasi-hydrostatic forces, respectively. Under the maximum quasi-hydrostatic force, the peak displacement of the flexible wall appears with a magnitude from 0.21 to 0.48 wave excursion, which exacerbates the wave overtopping and the von Mises stress in the wall for the tested impacts. Afterward, the flexible wall vibrates at a frequency very close to its natural frequency in vacuo, which is independent of the incident wave frequency (being different from the non-breaking periodic wave-induced motions). Finally, the effect of air compressibility for simulating the violent breaking wave impact with considerable air entrapment at a large scale is discussed. The findings in this study can support the design of existing and novel offshore and coastal structures with flexibility.

### 1. Introduction

Coastal and offshore steep-fronted deformable (both existing and novel) structures such as rubber or flexible membrane dams (Rane et al., 2019; Chanson, 1997), flexible breakwaters (Diamantoulaki et al., 2008; Michailides and Angelides, 2012), wave energy converters (Babarit, 2017; Collins et al., 2021), and Floating Production Storage and Offloading (FPSO) hulls (Murawski, 2005; Wang et al., 2014) are vulnerable to violent breaking wave impact. Structural deformation can occur during such wave-structure interactions, which poses challenges to structural integrity. Tremendous impact pressure with a short duration is often produced when waves are close to or directly break onto the structures. Tanimoto and Takahashi (1994) reported that the large impulsive pressure induced by extreme waves can cause large caisson breakwaters to slide several meters. Oumeraci (1994) analyzed reasons for 22 failure cases of vertical breakwaters, in which the most frequent and significant cause is the impact loading of

breaking waves. Breaking waves can also be developed in the offshore region through e.g., modulational instability (Melville, 1982; Li and Fuhrman, 2021). Therefore, understanding the temporal and spatial processes of breaking wave impact has important implications for designing and optimizing resilient coastal and offshore structures.

The impact exerted on a rigid wall due to breaking waves has been extensively investigated in the past decades. The variability of the impact showed strong sensitivity to incoming wave conditions (Raby et al., 2022; Ravindar et al., 2022). If the wave transitions from non-breaking to incipient breaking with a slightly inclined surface when it strikes the wall, a sharp pressure spike ranging from 1.0 to 2.5 times the maximum quasi-hydrostatic pressure can be observed (Bullock et al., 2007). This condition gives rise to the *slightly-breaking* impact as termed by Oumeraci et al. (2001). Bagnold (1939) first conducted an experimental study on different types of breaking wave impact on a vertical wall. The highest pressure was observed when a small air

\* Corresponding author.

E-mail address: [pearl.li@nus.edu.sg](mailto:pearl.li@nus.edu.sg) (Y. Li).

pocket was entrapped between the wave and the wall. At this impact instant, the wavefront was almost parallel to the wall. The wave crest then overturned and the wave trough rapidly accelerated to form a jet up the wall (Bredmose et al., 2009). Lugni et al. (2006) reported that the acceleration of the jet can exceed 1500g, where  $g$  is the gravitational acceleration. Besides, the impact pressure was localized in both spatial and temporal distributions (Kirkgoz, 1995; Kirkgoz and Aköz, 2005). The gap between the overturning crest and the wall was rapidly narrowing as the jet ‘flips’ through it. Thereby this physical event was termed *flip-through* or *low-aeration* impact (Cooker and Peregrine, 1990). When the wave appreciably overturns prior to hitting the wall, a large pocket of air can be entrapped between the breaker and the wall. This condition termed *high-aeration* can significantly affect the impact dynamics (Bullock et al., 2007). The peak pressure was often thought to be reduced due to the cushioning effect of the entrained (or entrapped) air (Bredmose et al., 2015). Conversely, the force and impulse exerted on the wall can be increased by the air entrapment because the high pressure is more widely distributed spatially and temporally (Peregrine et al., 2005; Bullock et al., 2007; Bredmose et al., 2009). Ravindar et al. (2019) characterized these types of breaking wave impact on a vertical seawall with a recurve based on a large-scale experiment, which indicated that the impact pressure strongly depends on the breaking type. As the wave height increases, the wave is already broken before reaching the wall, which is termed *broken-wave* impact (Oumeraci et al., 2001). The breaker can entrain large quantities of air to produce an aerated turbulent bore that strikes the wall. Bullock et al. (2007) indicated that this impact type is also significant in engineering practice due to its long duration. The above-mentioned four typical types of violent breaking impact generally show strong sensitivity to the incoming wave shapes. They can also significantly vary in nominally identical waves (i.e., with identical incident waves) due to the influence of the preceding waves (Bullock et al., 2007; Bredmose et al., 2009). Recently, a novel impact type of breaking wave was noticed by Ravindar and Sriram (2021) for waves with high steepness. The breaking wave collapses with a small air entrapment, which has characteristics similar to the *low-aeration* impact.

Hydroelasticity is an essential phenomenon for flexible structures subjected to a violent wave impact, wherein wave and structural dynamics need to be considered simultaneously. Hattori and Tsujioka (1996) conducted laboratory experiments on wall deflection responses to impulsive wave forces, in which both the impact forces and the wall’s natural frequency dominate the structural response. Likewise, Kim-moun et al. (2009) experimented on breaking wave interaction with a vertical flexible wall and showed that the wall’s vibration has a frequency close to its modal frequency. Based on this experiment, Sriram and Ma (2012) conducted a numerical reproduction using a fluid-structure interaction (FSI) model. The fluid and solid domains were solved by a meshless method and the finite element method (FEM), respectively. These two domains were near-strongly coupled (i.e., not fully-coupled, fluid particles maintain their positions from the end of the previous time step during FSI iterations) with a partitioned procedure. To reduce the computational cost, Kumar and Sriram (2020) extended this model to a hybrid scheme in which the fluid domain was divided into a far-field inviscid fluid and a near-structure viscous fluid. Tieleman et al. (2019) developed a semi-analytical model to quantify floodgate vibrations subjected to an impulsive wave impact. With the linear potential flow and structure assumptions, this model could provide computationally efficient results for a preliminary design. For modeling violent impacts with considerable air entrapment, especially for a large scale, multiphase flow simulations can provide better predictions of impact pressure on structures. Liao and Hu (2013) developed a coupled FSI model to simulate the tank sloshing with an elastic cantilever wall. The fluid domain considered as a multiphase field was solved by the finite difference method (FDM), which enabled the simulation of entrapped air dynamics. This model was further validated against an experiment on the dam-break wave impacts on an elastic

wall (Liao et al., 2015), wherein the experimental results indicated that the vibration modes of the wall were sensitive to the violent turbulent flow motion in the air cavity. Recently, a fully-coupled FSI model based on the finite volume method (FVM) was developed in the framework of OpenFOAM (Cardiff et al., 2018; Tuković et al., 2018), which can combine any fluid and solid models using a partitioned approach. This model has been developed and validated in previous studies on non-breaking wave interaction with flexible structures (Huang et al., 2019; Huang and Li, 2022; Hu et al., 2023; Attili et al., 2023). To date, violent breaking wave impacts on flexible steep-fronted structures and their underlying mechanisms have not been studied in a detailed manner.

For simulating breaking waves and their impacts on structures, Reynolds-averaged Navier–Stokes (RANS)-based turbulence models have been most widely used in previous studies. As a pioneer work, Lin and Liu (1998) numerically simulated spilling-type breaking waves employing a nonlinear  $k - \epsilon$  turbulence model ( $k$  is the turbulent kinetic energy, and  $\epsilon$  is the turbulent dissipation rate). However, over-production of turbulence was observed in both pre- and post-breaking regions in their simulations, leading to premature wave decay and inaccurate velocity fields. This is also seen in other recent works, e.g., Brown et al. (2016), Devolder et al. (2018). Larsen and Fuhrman (2018) demonstrated that RANS-based two-equation turbulence closure models were unconditionally unstable in the potential flow region beneath surface waves. They formally stabilized the two-equation models to avoid the unphysical over-production of turbulence in the pre-breaking regions. Fuhrman and Li (2020) likewise analyzed the realizable  $k - \epsilon$  turbulence model and found it is conditionally unstable in such regions and proposed a stabilized model. The stabilized two-equation models have achieved good accuracy in both the pre-breaking region and the outer surf zone, compared with the standard two-equation models. However, they were not capable of accurately predicting the hydrodynamics in the complicated inner surf zone (the region closer to the shoreline after breaking), as demonstrated in Larsen and Fuhrman (2018). More recently, Li et al. (2022) analyzed the Reynolds stress models (RSM), i.e., the Wilcox (2006) stress- $\omega$  model ( $\omega$  being the specific turbulent dissipation rate) and the Launder et al. (1975) stress- $\epsilon$  model. They were found to be neutrally stable in the potential flow region beneath surface waves. The theoretical superiority of the RSM model (i.e., breaking free from the Boussinesq approximation) also resulted in more accurate predictions of the turbulence and the undertow in the inner surf zone, and the breaking wave impact on a vertical pile (Li and Fuhrman, 2022). As the present study does not include the inner surf zone problem or flow around a bluff body (as those in Li et al. (2022), Li and Fuhrman (2022)), the stabilized two-equation turbulence model of Larsen and Fuhrman (2018) is applied in this paper, and should achieve sufficient accuracy as demonstrated in Sections 3.2–3.3.

The present study aims to investigate how hydroelasticity affects the four distinctive types of violent breaking wave impacts at a large scale using a fully-coupled computational model. The impacts include:

(i) *Slightly-breaking* impact: the transition from non-breaking wave impact to the fully-developed (i.e., with an appreciable sharp pressure spike characteristic) impact.

(ii) *Low-aeration* impact: the breaker adjacent to the wall contains relatively little air.

(iii) *High-aeration* impact: the breaker adjacent to the wall contains a large air pocket due to the entrapment.

(iv) *Broken-wave* impact: the incoming wave broke with a highly aerated turbulent bore before it reaches the wall.

The remainder of the paper is organized as follows. Section 2 describes the computational methods for modeling breaking waves and the flexible structure in a fully-coupled way. Thereafter, the computational model is validated against a large-scale experiment of Bullock et al. (2007) and a benchmark experiment of Liao et al. (2015), as in Section 3. Section 4 investigates the aforementioned impact types of breaking waves on a vertical flexible wall. The characteristics of

impacts and structural responses are presented and discussed. Section 5 provides a discussion on whether the air compressibility effects need to be considered for simulating the *high-aeration* impact at a large scale. Conclusions are drawn in Section 6.

## 2. Computational methods

The numerical model was implemented in [Hu et al. \(2023\)](#) which involves a computational fluid dynamics (CFD) model, a computational solid mechanics (CSM) model, and a fully-coupled scheme. In the present CFD model, as breaking waves on the porous rubble mound are modeled, the flow in the Cartesian coordinate system is simulated by solving the Volume-averaged Reynolds-averaged Navier-Stokes (VARANS) equations (see Eqs. [\(A.1\)](#) and [\(A.16\)](#)) with a stabilized  $k-\omega$  turbulence model (see Eqs. [\(A.6\)-\(A.13\)](#)) of [Larsen and Fuhrman \(2018\)](#), which are implemented in the present numerical model. Two-phase (water-air), immiscible, isothermal, and incompressible flow is considered in the present study. Our preliminary comparison study showed that air compressibility has little effect on the problem we investigated, thus, incompressible flow is considered, which will be further discussed in Section 5. The Volume of Fluid (VOF) approach ([Hirt and Nichols, 1981](#)) is applied for tracking the water-air interface. In the CSM model, the governing momentum equation for the solid is integrated over the initial undeformed configuration and referred to as a total Lagrangian approach. A nonlinear mechanical constitutive law, i.e., Neo-Hookean hyperelastic law implemented by [Cardiff et al. \(2018\)](#) is employed to calculate the Cauchy stress. A fully-coupled scheme implemented by [Tuković et al. \(2018\)](#) is employed for the solutions involving the fluid and solid domains based on a partitioned scheme, which is the same as that in [Hu et al. \(2023\)](#), and is briefly summarized herein ([Appendices A.2 and A.3](#)).

In the present study, the tolerance of the displacement residual (i.e., the relative displacement between the fluid side and solid side interfaces) is specified as  $1 \times 10^{-6}$  m which is a negligible value compared with the magnitude of the displacement. The maximum number of FSI iterations per time step is set as 200, which allows the convergence to be achieved in each time step ([Fig. B.19](#) in [Appendix B](#)).

## 3. Model setup and validation

In this section, the model setup is presented and the computational model is validated against the experiments in terms of (1) the violent breaking wave impact on a rigid wall and (2) the dam-break impact on a flexible wall.

### 3.1. Model setup

The two-dimensional computational domain used in Sections 3.2, 4, and 5 is set up according to the vertical wall tests in the large-scale experiment conducted by [Bullock et al. \(2007\)](#). The sketch of the numerical flume is presented in [Fig. 1](#). The  $x$ -axis points toward the wave propagation direction and the  $z$ -axis toward the vertically upward direction. Progressive waves are generated in the wave inlet boundary. The rubble mound in front of the wall is modeled as the porous media. The coefficients take the values  $\alpha_p = 500$ ,  $\beta_p = 2.0$ , and  $n = 0.49$  as suggested by [Jensen et al. \(2014\)](#), assuming a characteristic diameter of  $d_{50} = 0.25$  m. Three different bottom slopes are connected to represent the rubble mound profile digitized from the experiment. The vertical wall with a height ( $l$ ) of 3.0 m and a thickness ( $b$ ) of 0.15 m is mounted on the crest of the mound. The freeboard of the wall is  $h_f = l - h_s$ , where  $h_s$  is the still water depth at the wall ([Table 1](#)). Both the rigid and the flexible walls are simulated in the present study for comparison purposes. The density ( $\rho_s$ ) and Young's modulus ( $E$ ) of the rigid wall are 1800 kg/m<sup>3</sup> and 36.0 GPa, respectively, representing the reinforced concrete. For the flexible wall investigated in Section 4,

$\rho_s = 1200$  kg/m<sup>3</sup> and  $E = 0.258$  GPa, which can be considered a rubble-like structure. The corresponding natural frequency of the first mode in vacuo  $f_n$  is 1.25 Hz. The dimensionless parameter, Cauchy number  $Ca = \rho_w U_m^2 l^3 / EI$  (denoting the relative magnitude of the hydrodynamic forcing and the restoring effect of structural stiffness), ranges from 0.72 to 1.30 before the wave shoaling, where  $I = b^3/12$  is the moment of inertia of the wall. Waves downstream of the vertical wall are absorbed in the wave outlet boundary. To measure the wave surface elevation at various locations from the far field to the near-structure field, six wave gauges WG1-WG6 are placed and their positions in the wave propagation direction are -156.14, -13.29, -9.29, -5.29, -2.14, -0.02 m, and are illustrated in [Fig. 1](#). Meanwhile, the pressure along the vertical wall,  $P$ , is recorded. The horizontal force on the wall per unit width,  $F_x$ , is obtained by integrating the pressure measurements over the wall surface. The impact impulse,  $I_{imp}$ , is obtained by integrating the force values over the impact duration from the start of the impact to the first point that the force falls below the maximum quasi-hydrostatic force.

The computational domains for both fluid and solid are spatially discretized into finite volumes. Based on our preliminary grid convergence study, the computational mesh utilized in the fluid domain is 300 cells per wavelength and 30 cells per wave height in the far field. The mesh is refined around the wall with 60 cells per wave height and a cell aspect ratio of 1:1 ([Fig. 1](#)). Model validations with this mesh resolution also compared well with the experimental results in terms of the wave surface elevation, peak impact pressure, and horizontal forces on the wall, which will be shown in Section 3.2. The mesh in the solid domain is conformal to the fluid domain to reduce the interpolation error, resulting in a stable solution. Boundary and initial conditions in the present study are set as follows:

- (i) Wave inlet boundary: a wave generation boundary combined with active wave absorption, initialized with IHFOAM developed by [Higuera et al. \(2013\)](#), is employed. It prescribes free surface and velocities as Dirichlet boundary conditions from the stream function theory ([Fenton, 1988](#)). The pressure boundary condition sets the pressure gradient to the provided value such that the flux on the boundary is as that calculated with the specified velocity.
- (ii) Wave outlet boundary: a pure active wave absorption boundary is used. The velocities are prescribed from the absorption theory ([Higuera et al., 2013](#)) and the phase indicator  $\alpha$  is set as zero normal gradient at the boundary. The pressure boundary condition is the same as the wave inlet.
- (iii) Seabed boundary: a no-slip condition along with standard smooth bed wall functions are used. Both  $\alpha$  and pressure are set as zero normal gradient at the boundary.
- (iv) Atmosphere boundary: a zero-gradient condition is assigned for the flow out of the domain, and the velocity based on the flux in the patch-normal direction is employed for the flow into the domain.  $\alpha$  is again set as zero normal gradient. Pressure at the boundary is specified as the total pressure in excess of hydrostatic  $p_T^* = p_0^* - \frac{1}{2}\bar{u}_i^2$  ( $p_0^*$  denoting the reference pressure is set as zero herein).
- (v) Vertical wall boundary: the interfaces with solid are set as the Dirichlet boundary condition for the velocity together with the smooth bed wall functions. Both  $\alpha$  and pressure are again set as zero normal gradient. In the solid domain, the interfaces with fluid are specified as the Neumann boundary condition for the traction. The fixed-support boundary is prescribed at the bottom of the wall.

The initial turbulence field is set at a low level with the initial turbulent kinetic energy  $k_0 = 0.1 \omega v$  such that  $v_T/v = 0.1$ , combining with the initial specific dissipation rate  $\omega = 2.0 \text{ s}^{-1}$  following [Larsen and Fuhrman \(2018\)](#). In this work, the pressure-velocity coupling is solved using the PISO (Pressure Implicit with Splitting of Operators) algorithm ([Issa, 1986](#)). The maximum Courant number is set to 0.10.

Four cases ([Table 1](#)) corresponding to the aforementioned distinctive types of breaking wave impact are directly selected from the most severe cases in the experiment of [Bullock et al. \(2007\)](#), where  $H$  is

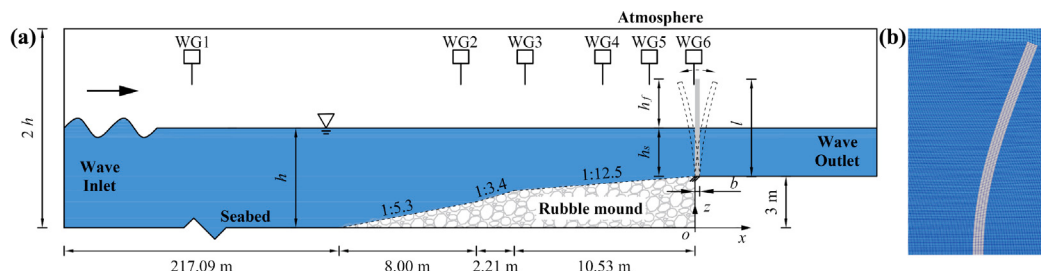


Fig. 1. (a) A sketch of the numerical flume with the gray cross denoting the bed profile of the rubble mound in the experiment of Bullock et al. (2007). (b) The zoom-in view of the deformed mesh in blue for the fluid domain and gray for the solid domain.

**Table 1**

Wave and structural properties in the present simulations.

Impact type	$H$ (m)	$T$ (s)	$h$ (m)	$h_s$ (m)	$h_f$ (m)	$Ca$
Slightly-breaking	1.25	8	4.25	1.25	1.75	0.79
Low-aeration	1.15	8	4.00	1.00	2.00	0.72
High-aeration	1.25	8	4.00	1.00	2.00	0.90
Broken-wave	1.50	6	3.70	0.70	2.30	1.30

the wave height,  $T$  is the wave period, and  $h$  is the water depth. For each rigid/flexible case, a passage of 10 waves takes approximately 0.2/2 days using 48 processors on the supercomputer of the National Supercomputing Centre (NSCC) Singapore.

### 3.2. Model validation against Bullock et al. (2007)

To validate the present numerical model, the *high-aeration* impact case (as in Table 1) of Bullock et al. (2007) is reproduced. The impact of the first fully-developed wave is used for comparisons that follow. First, the comparison of the wave surface elevation ( $\eta$ ) between the computational and the experimental results are shown in Fig. 2, where  $t_0$  is the start instant for sampling. Also, the numerical results of Liu et al. (2019) are presented as a comparison. In their study, the rubble mound was considered an impermeable wall, and its profile was simplified as two connected slopes (instead of three in the present study). Fig. 2 shows reasonably good agreement at different locations between the present study and the experimental results. The wave elevations predicted with the present model at WG1 close to the wave inlet boundary as well as WG2 near the junction of the first and second rubble slopes perfectly agree with the experiment, while Liu et al. (2019) showed discrepancies at WG1 and WG2. Wave reflections due to the structure are also reasonably captured at WGs2–5 with the present model, observed as the second peak in Fig. 2b-d. Overall, the present study predicts better results in Fig. 2a-d, especially for the phase and the amplitude of the reflected wave, compared with Liu et al. (2019). In Fig. 2e, both numerical results at WG5 are comparable to the experimental data. In Fig. 2f, the present study predicts higher amplitude at WG6 (the nearest gauge to the wall) than the experiment and Liu et al. (2019). This may be owing to the two-dimensional set-up in the numerical study, where the wave does not transfer in the transverse direction as that in the experiment. It is also noted that Liu et al. (2019) used a ramp-up time (i.e., the duration for waves to vary from 0 to the target value) of  $4T$  for the wave generation while their results were recorded from  $2T$  after the initial wave reached the wall. Thus, their results may not have been fully developed.

The spatial distributions of the peak pressure,  $P_{z,max}$ , along the vertical rigid wall subjected to the *high-aeration* impact from numerical predictions and measurement are compared in Fig. 3a. The present simulation successfully captures the profile of peak pressure. The prediction for the pressure distribution is much improved compared with that of Liu et al. (2019), especially for the impact region, although they used a compressible flow model. The horizontal force per unit width,  $F_x$ , is compared in Fig. 3b. In the experiment,  $F_x$  is obtained

by integrating the pressure measurements over the vertical extent on the wall. For comparison,  $F_x$  is calculated in the same way in our numerical simulations. Fig. 3b shows that the predicted  $F_x$  matches well with the experimental measurement. The magnitude of the impact force is slightly overestimated due to the overestimation of the wave amplitude near the vertical wall, as shown in Fig. 2f. In addition, the impact duration/impulse is underestimated and the sub-atmospheric pressure associated with the air expansion is not reproduced because of the incompressible air assumption in the present study, which will be discussed in Section 5. The force oscillations after the main peak were captured but much overestimated in both amplitude and duration in Liu et al. (2019). Overall, the present model with incompressible flow assumption can achieve good predictions of the wave elevation, peak pressure distribution, impact force, and quasi-hydrostatic force.

### 3.3. Model validation against Liao et al. (2015)

Section 3.2 validates the capability of the present numerical model to simulate the breaking wave impact on a rigid wall. To further validate the modeling of the structural response of an elastic wall under the violent wave impact, a benchmark experiment conducted by Liao et al. (2015), who investigated the interaction between the dam-break wave and an elastic wall at a small scale is numerically reproduced. An illustration of the initial condition in the experiment and the present simulation is shown in Fig. 4. The initial water column is 0.4 m high and abruptly released to form a dam-break wave. The elastic wall made of silicon solid rubber is fixed at the tank bottom. It has a density ( $\rho$ ) of 1161.54 kg/m<sup>3</sup>, Young's modulus ( $E$ ) of 3.50 MPa, and Poisson's ratio ( $\nu$ ) of 0.49. The height ( $l$ ) and thickness ( $b$ ) of the wall are 0.09 m and 0.004 m, respectively. The horizontal displacements,  $D_x$ , of the wall at vertical locations of 0.04 m, 0.065 m, and 0.0875 m from the bottom are compared in Fig. 5a. The computed  $D_x$  with the present model is in good agreement with the experimental measurement. Both the negative displacement at the initial impact stage and the maximum displacement are successfully reproduced. Moreover, the present model shows reasonable predictions for the free surface profile and the structural deformation at typical time instants in Fig. 5b. Based on the above validations, the present model is considered capable of accurately predicting violent breaking wave impacts on flexible structures.

## 4. Results and discussion

In this section, four distinctive types of violent breaking wave impact on a vertical elastic wall are investigated. The layout of the numerical setup is shown in Fig. 1, the same as the case of the vertical wall in the large-scale experiments of Bullock et al. (2007). The characteristics of the wave impact and structural response are analyzed.

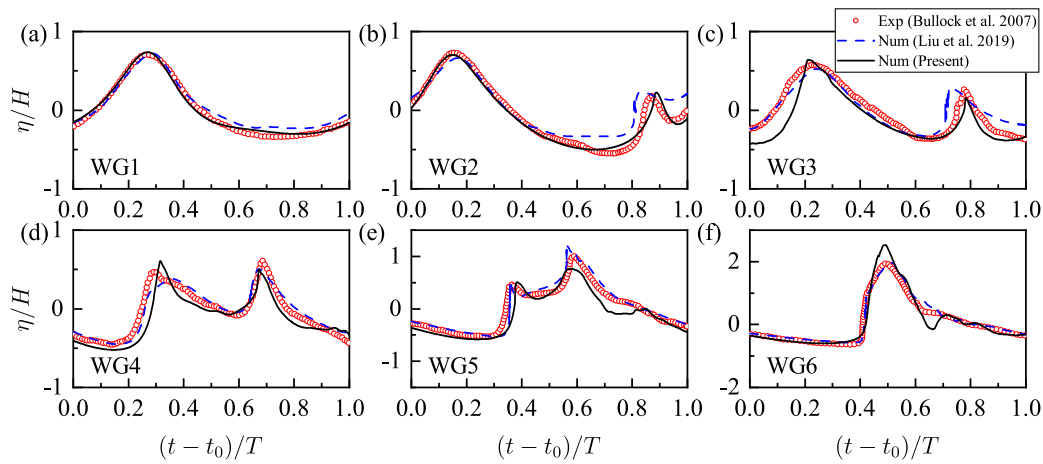


**Fig. 2.** Comparisons of wave surface elevations at different locations from the numerical simulations and the experimental measurement.

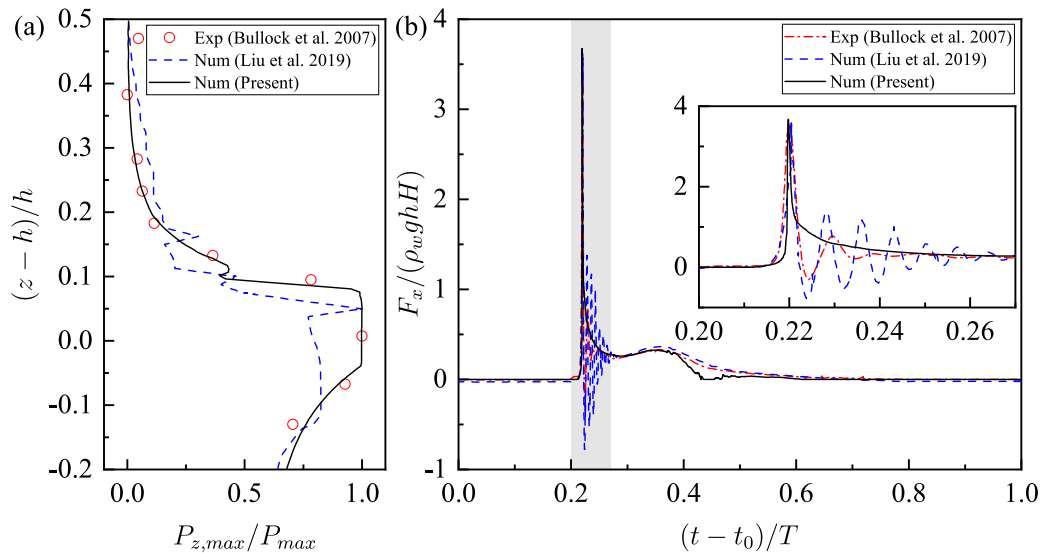


**Fig. 3.** Comparisons of (a) the spatial distribution of the peak pressure and (b) the horizontal force on the wall between the computations and the experiment.

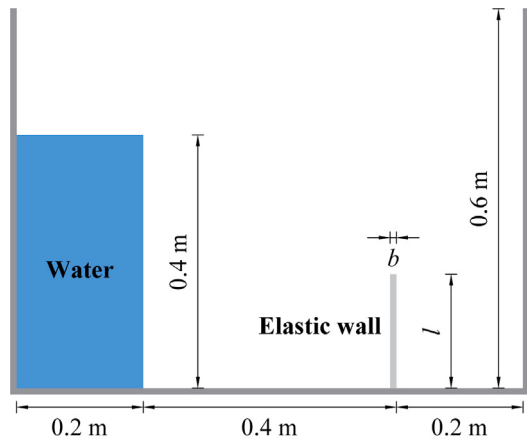


**Fig. 4.** A layout of the initial condition in the experiment of Liao et al. (2015) and the present simulation.

#### 4.1. Slightly-breaking wave impact

In this subsection, *slightly-breaking* impact on a rigid wall and a flexible wall is simulated and compared. Fig. 6 presents spatial profiles of the impact pressure on both rigid and flexible walls in one wave cycle. The peak pressure is highly localized and with a profile like a church spire. The highest value of the peak pressure along the rigid wall occurs at the location where the wavefront strikes the wall, i.e.,  $(z - h)/h = 0.1$ . This high pressure then propagates away from the impingement point. The pressure rapidly decreases on both sides. Specifically,  $P_{z,max}$  is around  $0.45P_{max}$  and almost uniform below the still water level. It approaches approximately  $0.01P_{max}$  when  $(z - h)/h > 0.2$ . For the flexible wall, the peak pressure distribution shows a similar trend to that of the rigid wall. However, the highest peak pressure moves up since the flexible wall is slightly deflected under the peak impact force, which is also observed in other impact types as in the following sections. It implies that the stagnation point where the flow velocity is equal to zero shifts upward on the deformed wall. The pressure wave is easier to propagate up but more difficult to go down on the inclined wall. Therefore, the peak pressure values are generally higher above the wave impingement point and lower beneath it compared with the rigid wall. For the flexible wall,  $P_{z,max}$  is around  $0.40P_{max}$  below the still

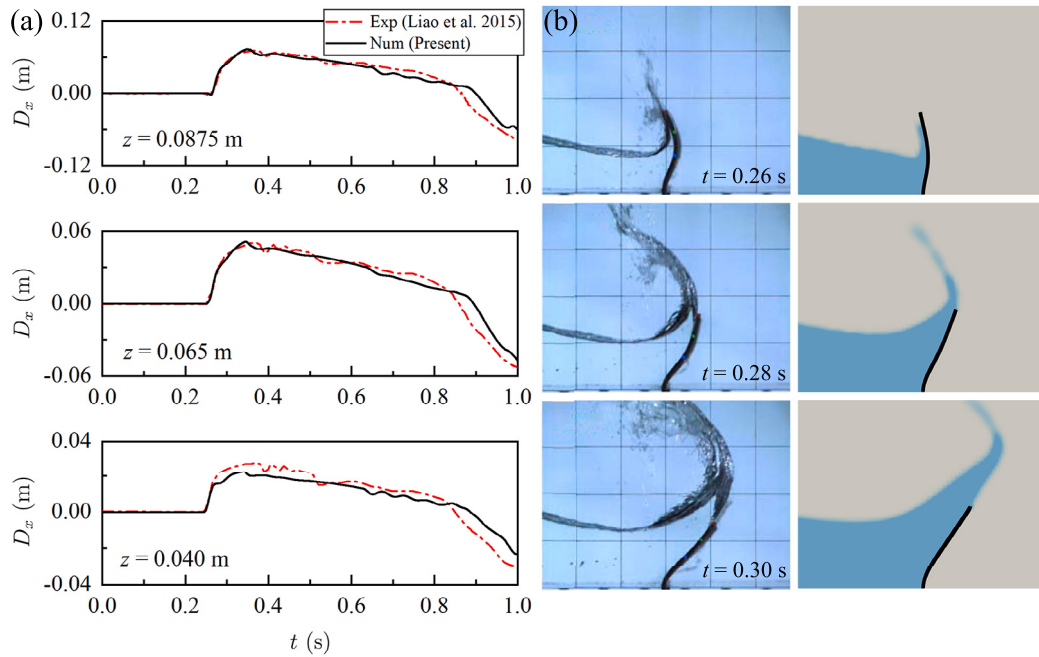


**Fig. 5.** Comparisons of (a) structural displacements and (b) free surface profile and structural deformation between the computational results and the experimental measurement.

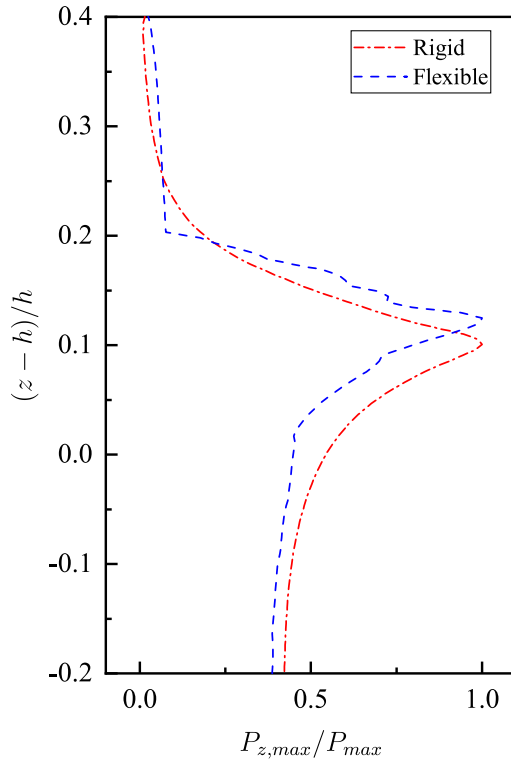


**Fig. 6.** Comparison of the spatial distribution of the peak pressure between the rigid and flexible walls subjected to the *slightly-breaking* impact.

water level and approaches approximately  $0.04P_{max}$  when  $(z - h)/h > 0.2$ .

Fig. 7 presents the temporal series of the total force on both the rigid and the flexible walls. The sharp spike and the secondary bump after the main impact peak in the horizontal force,  $F_x$ , are known as the impact and quasi-hydrostatic forces, respectively. It is seen that the impact peak is reduced on the flexible wall compared with the

rigid one. For the rigid wall, the magnitude of the impact force is  $1.63\rho_w g h H$  at the impact instant  $t_a$  and 3.98 times the maximum quasi-hydrostatic force at the time instant  $t_c$ . The impact duration is about  $0.043T$  including the rise time and the fall time. The impact impulse ( $I_{imp}$ ) on the wall throughout the impact duration is 8.42 kNs/m, see Table 2. Afterward, low amplitude pulsations of the total force are observed due to the wave-overtopping induced splash downstream of the wall. For the flexible wall, the magnitude of the impact force is  $1.35\rho_w g h H$  at the impact instant  $t'_a$  and 2.94 times the maximum quasi-hydrostatic force. Moreover, the impact duration decreases  $0.012T$ , which naturally results in that  $I_{imp}$  reduces to 4.92 kNs/m. Note that the maximum quasi-hydrostatic force reaches earlier for the flexible wall because the wavefront is easier to move up on the inclined wall. The horizontal displacement of the free top,  $D_x$ , is normalized by the wave excursion,  $A_w = u_m T / 2\pi$ . It can be seen that the structural deformation is initialized when the wave just hits the wall.  $D_x$  increases and reaches its maximum,  $0.48A_w$ , at the time instant  $t_b$  around the maximum quasi-hydrostatic force. After that, the flexible wall starts to restore with the decrease of the quasi-hydrostatic force. Finally, the wall vibrates at the wet natural frequency  $f_{Dx}$  very close to the structural natural frequency in vacuo since the main structural vibrations occur outside the water. This is also observed in other impact types that follow. It is different from the cases of non-breaking periodic waves, in which the flexible wall tends to vibrate at the wave frequency (Hu et al., 2023). The latter is because the structural natural frequency is much higher than the incoming wave frequency so that the non-breaking periodic waves are less likely to excite the high-frequency vibration of structures.

Fig. 8 presents the wave profiles, turbulence levels, and structural responses at several typical time instants ( $t_a$ ,  $t'_a$ ,  $t_b$ , and  $t_c$ , as in Fig. 7) during the impact process for both the rigid wall (upper panels) and the flexible wall (lower panels). Note that  $t_a$  and  $t'_a$  correspond to the impact peak for the rigid and the flexible cases, respectively, and  $t_b$  and  $t_c$  correspond to the maximum displacement for the flexible case and the maximum quasi-hydrostatic force for the rigid case, respectively. In Figs. 8a and d, at the time instant of the impact peak, the wave just collides with the wall front for both the rigid and the flexible cases. In this region, no air is entrapped between the slightly inclined wavefront and the vertical walls. The contraction of the free surface

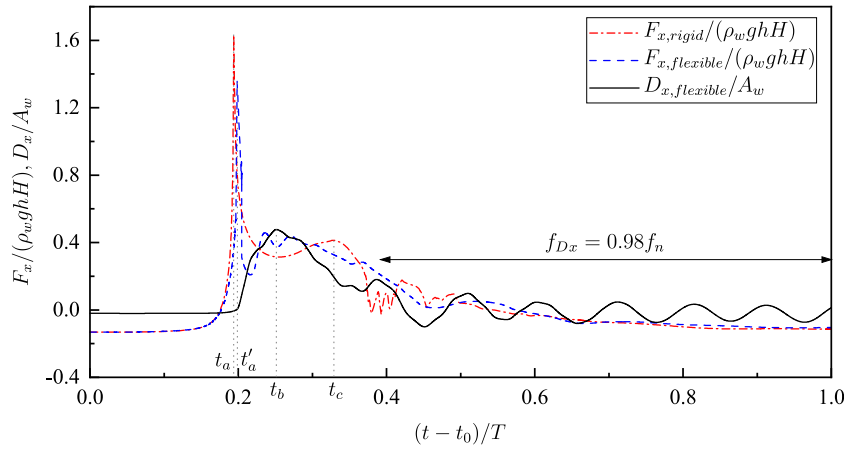


**Fig. 7.** Comparisons of the temporal evolution of horizontal force and the corresponding structural displacement between the rigid and the flexible walls subjected to the *slightly-breaking* impact.

**Table 2**  
The impact impulse ( $I_{imp}$ ) on the wall during different impact events.

Wall	Slightly-breaking	Low-aeration	High-aeration	Broken-wave
Rigid (kNs/m)	8.42	6.63	8.06	1.18
Flexible (kNs/m)	4.92	3.17	5.04	2.92

leads to an abrupt pressure rise with the converging flow. There is no significant turbulence production beneath the free surface, apart from minor in the vicinity of the impact region and the boundary layer region on the rubble mound for both the rigid and the flexible cases. The turbulence production is contributed by the relatively large velocity gradient (Lin and Liu, 1998). At the time instant  $t_b$  (Figs. 8b and e), the highest displacement of the flexible wall is reached under the maximum quasi-hydrostatic force. The pressure gradient accelerates the water jet to shoot up from the impact area. Note that the deformation of the flexible wall transfers part of the momentum in the horizontal direction, whereas the rigid wall transfers all upward. At the time instant  $t_c$  (Figs. 8c and f), the quasi-hydrostatic force on the rigid wall is reached. The water flows over the wall, where the wave-overtopping volume is larger for the flexible case.

The distribution of von Mises stress,  $\sigma_v$  (normalized by  $\rho_w g H$ ), in the walls subjected to the *slightly-breaking* impact is also shown in Fig. 8. At the time instant of the impact peak, it is seen that more pronounced  $\sigma_v$  is located at the impact region and the toe of the wall (Figs. 8a and d). Moreover,  $\sigma_v$  in the flexible wall is generally smaller than that in the rigid wall, which is also observed in the following *low-aeration* and *high-aeration* impacts. For the rigid wall, the maximum  $\sigma_v$  occurs around the peak impact force and then becomes insignificant after the impact event. However,  $\sigma_v$  in the flexible wall reaches its peak under the maximum quasi-hydrostatic force, especially for the front and back sides beneath the wave impingement point. It then gradually decreases with the restoration of the flexible wall. These indicate that the structural integrity of the rigid wall is more vulnerable to the peak impact force, whereas the structural integrity of the flexible wall is more susceptible to the maximum quasi-hydrostatic force.

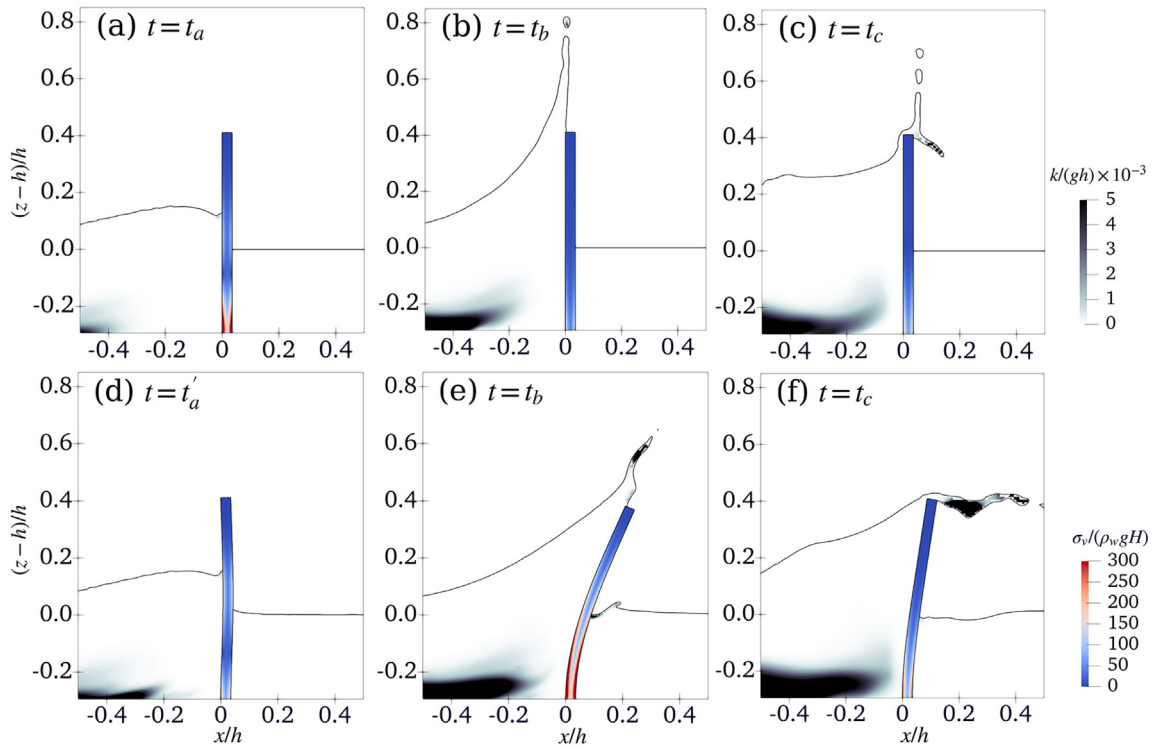
#### 4.2. Low-aeration impact

The wave for the *low-aeration* impact approaches the wall with a more developed wavefront and little air entrainment. Fig. 9 provides a comparison of the impact pressure distribution between the rigid and the flexible walls. The peak pressure is more spatially localized compared with that under the *slightly-breaking* impact for both rigid and flexible cases. The highest peak pressure is located at the wave impingement point, i.e.,  $(z - h)/h = 0.086$  and  $(z - h)/h = 0.102$  for the rigid and flexible walls, respectively. A sudden pressure drop occurs

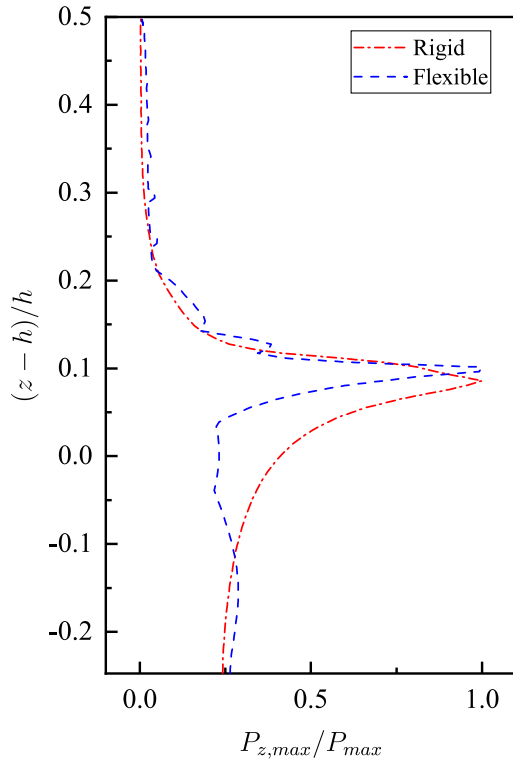
above and beneath this point. Note that some discontinuities in  $P_{z,max}$  for the flexible wall are seen, which might be induced by the local pressure oscillations related to the mesh deformation.

Fig. 10 presents the comparison of the total force between the rigid and the flexible walls. Compared to that with the *slightly-breaking* impact, the impact forces increase and become more temporally localized for both the rigid and the flexible walls. Specifically, the magnitude of the impact force exerted on the rigid wall is  $3.32\rho_w g h H$  and 8.98 times the maximum quasi-hydrostatic force. The flexibility of the wall seems to present an effective cushioning effect: The peak impact force decreases to  $2.05\rho_w g h H$  and 4.66 times the maximum quasi-hydrostatic force. The impact durations generally become shorter than the *slightly-breaking* impact. It decreases about  $0.004T$  for the rigid wall case and  $0.007T$  for the flexible wall case, respectively. Consequently, the impact impulse on the wall reduces although the peak force increases comparing between the *slightly-breaking* impact and *low-aeration* impact cases, see Table 2. Also, the highest structural displacement,  $D_x = 0.38A_w$ , occurs around the time instant of the maximum quasi-hydrostatic force for the flexible wall. The highest  $D_x$  is significantly lower when compared with the *slightly-breaking* impact, which indicates the magnitude of the structural deformation is more dependent on the quasi-hydrostatic force, rather than the peak impact force.

Fig. 11 shows the wave profiles, turbulence levels, and structural responses for the *low-aeration* impact at the typical time instants ( $t_a$ ,  $t'_a$ ,  $t_b$ , and  $t_c$ , as in Fig. 10). In Fig. 11a, at the time instant of the impact peak, the wavefront presents a nearly vertical profile that is parallel to the rigid wall, with a typical feature of the *flip-through* impact. The flow with high velocity converges on the highly confined impact zone. Fig. 11d shows that the deformation of the flexible wall produces slightly different wave profiles for the nominally identical waves. The different reflections from the preceding waves caused by the rigid and the flexible walls result in such variability of the wave impact. The aerated area has the strongest turbulent kinetic energy and other regions are nearly potential flow for both the rigid and the flexible cases. At the time instant  $t_b$  (Figs. 11b and e), with the passage of the wave, a violent water jet driven by the pressure gradient is formed along the rigid and deformed walls. The turbulent kinetic energy in the turbulent bore front spreads out, and the main turbulence confines within the tongue of the upward jet. At the time instant  $t_c$  (Figs. 11c and f), the wave overtopping volume is close to zero for the rigid case but



**Fig. 8.** Wave profiles, turbulence levels, and structural responses at typical time instants for the *slightly-breaking* impact. (a–c) Rigid wall. (d–e) Flexible wall.



**Fig. 9.** Comparison of the spatial distribution of the peak pressure between the rigid and the flexible walls subjected to the *low-aeration* impact.

exacerbated by the wall deformation for the flexible case. The turbulent kinetic energy in the wavefront is obviously dissipated on the top of the rigid wall. Instead, it propagates downstream accompanied by wave overtopping for the flexible case.

At the time instant of the impact peak,  $\sigma_v$  in both the rigid and the flexible walls increases, especially at the impact region and the toe of the wall comparing between the *slightly-breaking* impact and *low-aeration* impact cases. This is due to the increased peak impact force, as seen in Fig. 10 compared with that in Fig. 7. Again,  $\sigma_v$  in the rigid wall decreases to negligibly small after the peak impact force, while the maximum quasi-hydrostatic force dominates the highest  $\sigma_v$  in the flexible wall.

#### 4.3. High-aeration impact

The wave for the *high-aeration* impact is more developed when compared to the *low-aeration* impact, i.e., it approaches the wall with a more overturned wavefront and a relatively large air pocket entrapment. The wave parameters for this impact are similar to the *low-aeration* impact with an increased incident wave height from 1.15 m to 1.25 m. Fig. 12 presents the comparison of the impact pressure between the rigid and the flexible cases. The distribution of the peak pressure over one wave period no longer looks like a church spire and is more uniformly distributed around the entrapped air pocket. The highest peak pressure spreads over a range from  $(z - h)/h = -0.04$  to  $0.07$  on the rigid wall. It is noted that a small spike occurs at  $(z - h)/h = 0.11$ , which might be induced by the evolution of the air pocket. The peak pressure rapidly decreases and reaches a stable value at higher locations.

Fig. 13 shows the total force on both the rigid and the flexible walls subjected to the *high-aeration* impact. It is seen that the impact force amplitude increases when compared to the *low-aeration* impact in Fig. 10. The maximum total force on the rigid wall is  $3.68\rho_w g h H$  and around 11.5 times the maximum quasi-hydrostatic force, which is the most extreme peak force among all cases in the present study. When the flexibility is introduced to the wall, the maximum total force decreases to  $2.58\rho_w g h H$  and 6.14 times the maximum quasi-hydrostatic force. The impact durations of the rigid and the flexible cases are nearly the same as those in the *low-aeration* impact cases. Thus, the impact impulse values for both the rigid and the flexible walls are larger than those under the *low-aeration* impact. It confirms what Bullock et al.

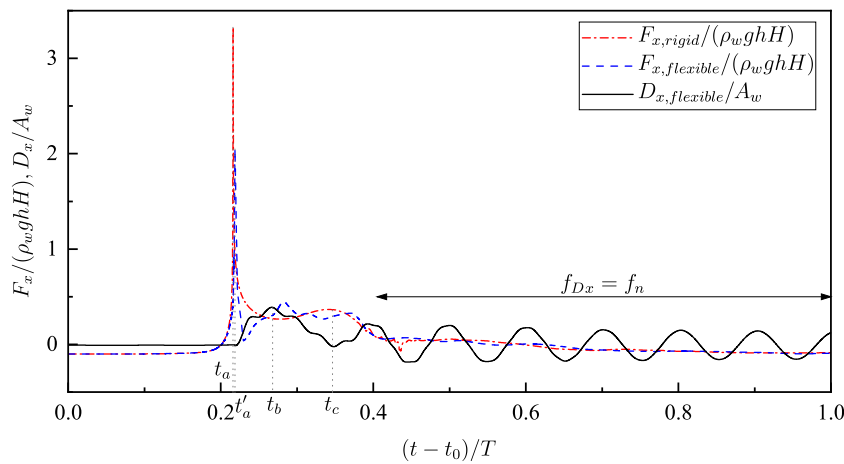


**Fig. 10.** Comparisons of the temporal evolution of horizontal force and the corresponding structural displacement between the rigid and the flexible walls subjected to the low-aeration impact.

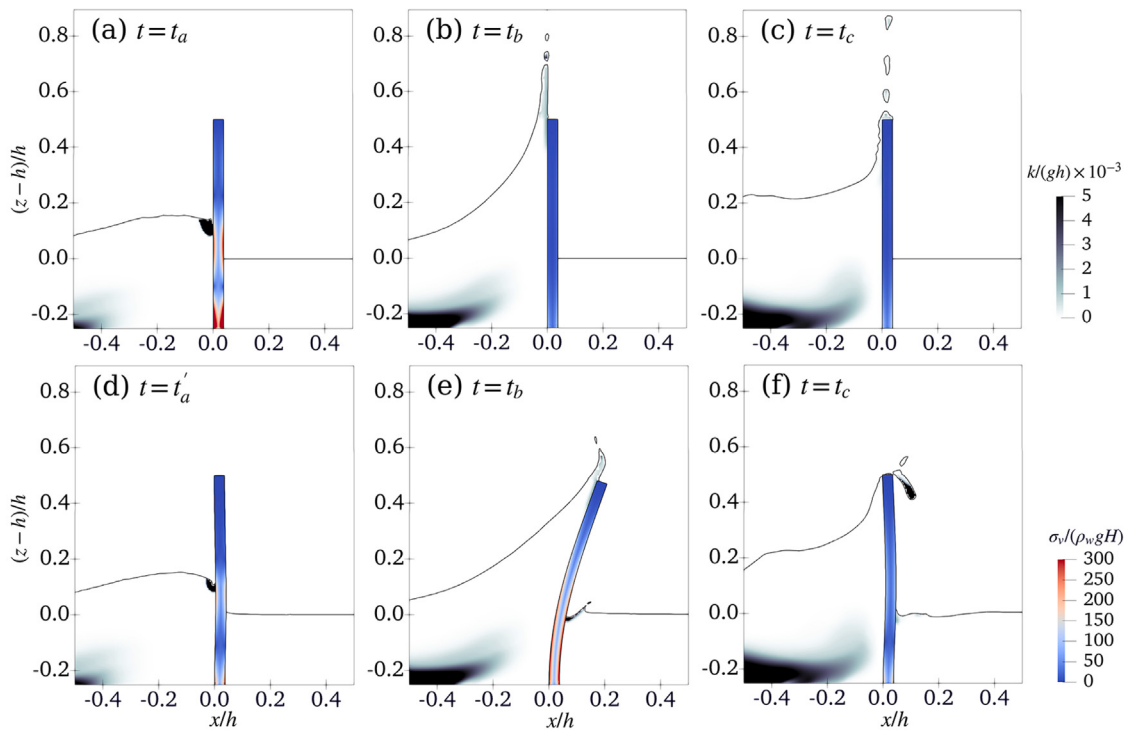


**Fig. 11.** Wave profiles, turbulence levels, and structural responses at typical time instants for the low-aeration impact. (a–c) Rigid wall. (d–e) Flexible wall.

(2007) pointed out that the air entrainment could increase the impact impulse on the structure. Again, the largest displacement of the flexible wall is induced by the maximum quasi-hydrostatic force. The maximum  $D_x$  in Fig. 13 is almost the same as that with the low-aeration impact in Fig. 10. This is mainly because the quasi-hydrostatic forces of these two cases are both around  $0.42\rho_w g h H$ .

Fig. 14 presents the wave profiles, turbulence levels, and structural responses at several typical time instants ( $t_a$ ,  $t'_a$ ,  $t_b$ , and  $t_c$ , as in Fig. 13) with the high-aeration impact. In Figs. 14a and d, at the time instant of the impact peak, a large air pocket is entrapped between the overturned wave crest and the walls in the vicinity of the wave impingement point. The highest turbulent kinetic energy almost occupies the entire breaking wavefront. At the time instant  $t_b$  (Figs. 14b and e), with the passage of the wavefront, the air cavity is evolved into an elongated shape and carried by the upward flow. The water with high turbulence intensity surrounds the entire cavity due to vertical diffusion. Some wiggles are

observed on the surface of the air pocket, especially for the flexible case. At the time instant  $t_c$  (Figs. 14c and f), the wave overtopping volume again increases with the introduced structural flexibility. The air pocket remains entrapped on the rigid wall while released for the flexible wall. For the rigid wall, a splash phenomenon appears in the air cavity as the air pocket is gradually depressurized. The turbulence intensity near the cavity is reduced and it starts spreading down. Instead, the deformation of the flexible wall facilitates the escape of the air pocket.

It is also observed that at the time instant of the impact peak, the water impact area and the enclosed air pocket are pressurized, which produces a larger  $\sigma_v$  near the impact area in the wall when compared to the low-aeration impact.  $\sigma_v$  in the flexible wall is generally smaller than that in the rigid wall. Again, the extreme  $\sigma_v$  appears under the peak impact force and the maximum quasi-hydrostatic force for the rigid and flexible walls, respectively.

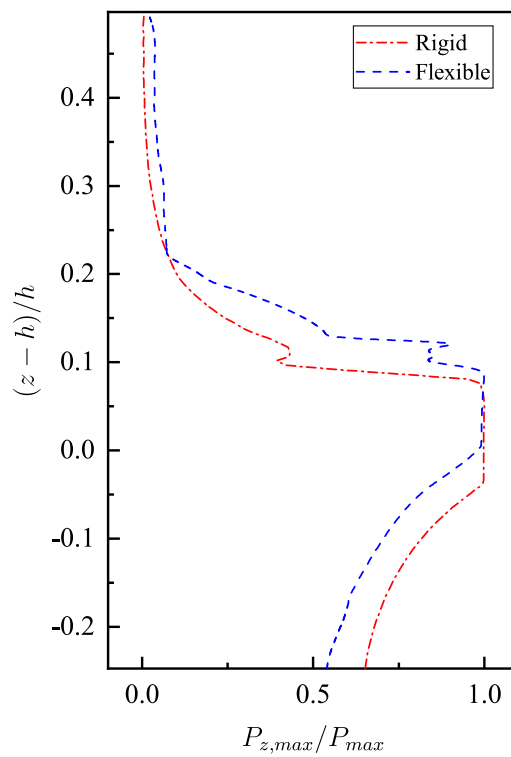


**Fig. 12.** Comparison of the spatial distribution of the peak pressure between the rigid and the flexible walls subjected to the *high-aeration* impact.

#### 4.4. Broken-wave impact

When the incident wave steepness significantly increases from 0.026 to 0.045, the wave on the rubble mound breaks before it reaches the wall, and produces a *broken-wave* impact. Fig. 15 presents the spatial distribution of the impact pressure on the wall. The peak pressure on both the rigid and the flexible walls shows a profile quite similar to that with the *high-aeration* impact. The highest peak pressure on the rigid wall occurs below the still water level, which is consistent with the result of Liu et al. (2019). It spreads within a range where the air pocket is entrapped.

Fig. 16 presents the temporal evolution of the total force. The peak impact force on the rigid wall is much lower than those of the aforementioned impact types. It is only  $0.65\rho_wghH$  and around 2.1 times the maximum quasi-hydrostatic force. However, the duration of the entire wave loading including the impact and the quasi-hydrostatic forces is longer than other impact types. That is, the *broken-wave* loading has a relatively high spatial and temporal span. For the flexible wall, the impact arrives later than that for the rigid case. Unlike other impact types, the highest impact force on the flexible wall slightly increases compared to that on the rigid wall. It is  $0.85\rho_wghH$  and approximately 3.15 times the maximum quasi-hydrostatic force. Also, the impact duration increases from  $0.013T$  of the rigid case to  $0.025T$  of the flexible case. Therefore, the flexible case has a larger impact impulse. This is because stronger wave reflections from a rigid wall cause the wave to break up earlier, and more energy is dissipated before reaching the wall. Note that the impulse with the *broken-wave* impact is the least significant among all studied impact types, as presented in Table 2.

Fig. 17 presents the wave profiles, turbulence levels, and structural responses at the typical time instants ( $t_a$ ,  $t'_a$ ,  $t_b$ , and  $t_c$  in Fig. 16) with the *broken-wave* impact. Figs. 17a and d show that the largest incident wave height among all the present wave cases, i.e., 1.5 m, breaks to wavelets with smaller amplitude. High turbulent kinetic

energy is produced beneath the highly aerated broken bore, extracting energy from the incident wave, making it less likely to produce a more violent impact on the wall compared to other impact types. The *broken-wave* impact case illustrated here looks like a weakened *high-aeration* impact since large air pockets are entrapped adjacent to the wall. The difference is that some air pockets are formed in the wave roller region (i.e., the recirculating flow in the front of the turbulent bore) before reaching the wall. The wave crest in the rigid case is below the still water level, which results in the peak pressure distribution in Fig. 15. Fig. 17a and d also show a pronounced variability of wave profiles for the rigid and the flexible cases in nominally identical waves. Such variability is well-known and is attributed to the difference in the reflection and the turbulence left from the preceding waves between the rigid and the flexible walls (Bullock et al., 2007). At the time instant  $t_b$  (Figs. 17b and e), a cloud of air pockets is evolved in the wavefront and pushed upward. These air pockets tend to merge and become elongated, similar to that in the *high-aeration* impact case. Turbulence intensity is diffused across the field of view beneath the wave surface. At the time instant  $t_c$  (Figs. 17c and f), similar to the *low-aeration* impact, wave overtopping is only observed in the flexible case. The turbulence intensity generally decreases and tends to transport upstream with the propagation of the reflected waves. It is noted that the vibration of the flexible wall evokes mild waves with high frequencies and small amplitudes downstream of the wall. This phenomenon is also observed with the other impact types in the present study.

At the time instants of the impact peak and the maximum quasi-hydrostatic forces for the rigid and the flexible walls (i.e.,  $t_a$ ,  $t'_a$ ,  $t_b$ , and  $t_c$ ),  $\sigma_v$  in both the rigid and the flexible walls behave similarly to but less significantly than those in other impact types.

#### 5. Discussion: “compressible” vs. “incompressible” air assumptions

This section discusses whether the air compressibility effects should be considered for simulating the violent breaking wave impact with considerable air entrapment at a large scale. As in the present study, the incompressible flow solver (i.e., *interFoam* in OpenFOAM version foam-extend 4.0) is used in the fluid model for both the water and the air phases, it could be useful to provide a brief discussion on why we adopted the incompressible flow assumption for this study. In fact, our initial study has incorporated a compressible solver (i.e., *compressibleInterFoam*) in the present fully-coupled model. The comparison of the results between using the compressible and the incompressible flow solvers, as well as the pros and cons of incorporating air compressibility in the model, are discussed in this section.

It is noted that Fig. 3b cannot directly demonstrate the differences between using a compressible and an incompressible solver. It is because in Liu et al. (2019), besides applying a compressible assumption for the fluid phase, their model setup (e.g., slope profiles, considering the rubble mound as an impermeable wall) and data sampling (i.e., the results were recorded during the wave ramp-up time) are also different from the present study. Therefore, to elucidate differences between the compressible and incompressible flow models, and to ensure full consistency of all other factors, the case of *high-aeration* impact on a rigid wall is simulated with the present model and setups incorporating the air compressibility. The time series of the horizontal force computed with the compressible flow solver (using exactly the same setup as that in Section 3) is shown in Fig. 18.

To consider the compressibility of the fluid, the mass continuity equation (Eq. (A.1)) becomes:

$$\frac{\partial \rho}{\partial t} + \frac{\partial \rho \bar{u}_i}{\partial x_i} = 0 \quad (1)$$

and the transport equation for each phase indicator  $\alpha$

$$\frac{\partial \rho \alpha}{\partial t} + \frac{\partial \rho \bar{u}_i \alpha}{\partial x_i} = 0 \quad (2)$$

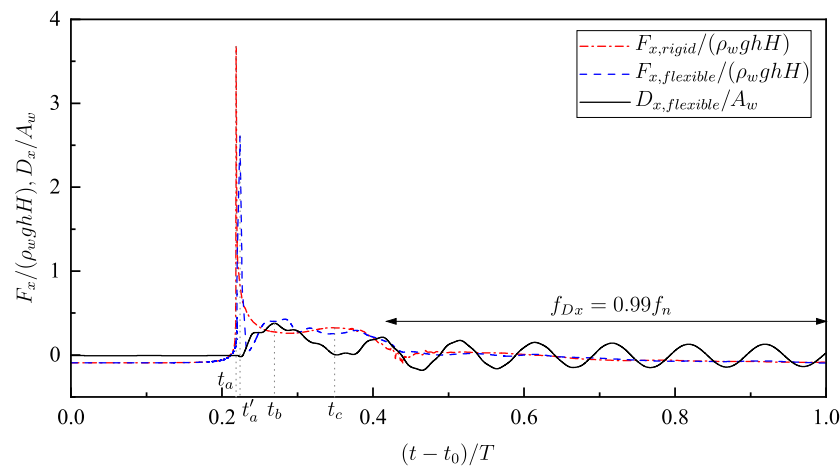


**Fig. 13.** Comparisons of the temporal evolution of horizontal force and the corresponding structural displacement between the rigid and the flexible walls subjected to the high-aeration impact.

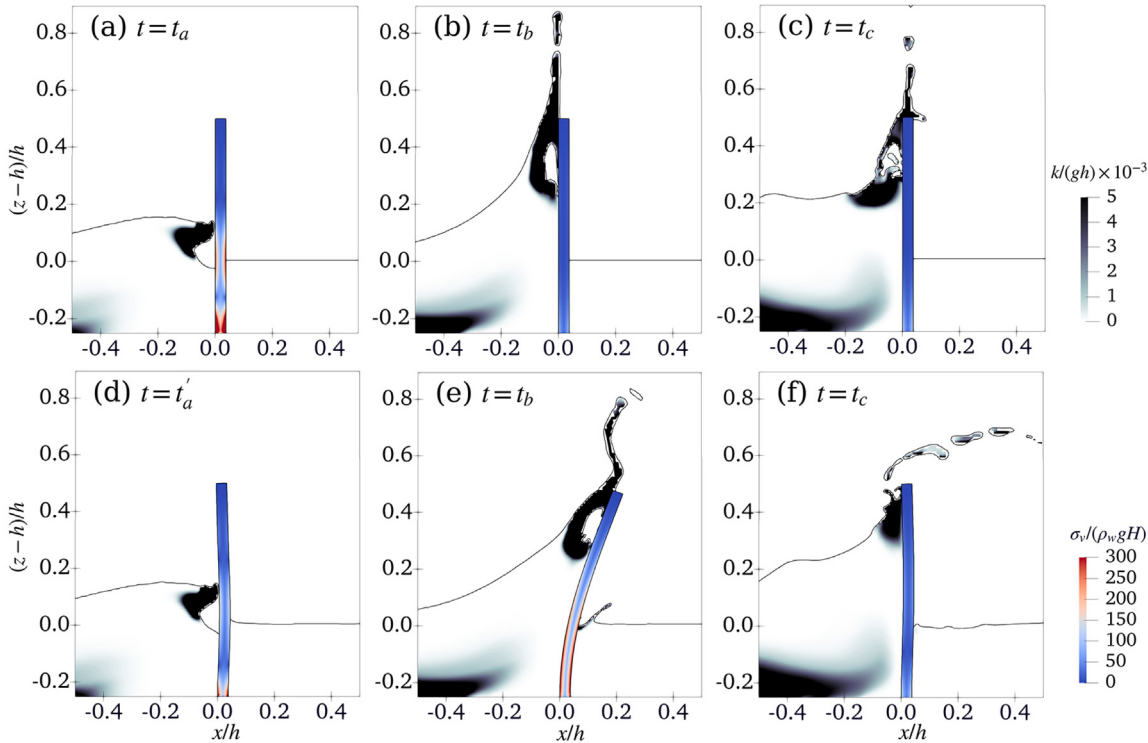


**Fig. 14.** Wave profiles, turbulence levels, and structural responses at typical time instants for the high-aeration impact. (a–c) Rigid wall. (d–e) Flexible wall.

For the compressible air phase, the total derivative of density with respect to the pressure for the ideal isentropic gas is given from the equation of state:

$$\frac{\partial \rho_a}{\partial p} = \frac{1}{a_c \gamma_c} \left( \frac{p}{a_c} \right)^{\frac{1-\gamma_c}{\gamma_c}} \quad (3)$$

where  $\gamma_c = 1.4$  is the ratio of specific heat and  $a_c = 1 \times 10^5$  is the isentropic constant in the present study. The isothermal equation of state specifies the density of the air phase using the pressure, and the energy equation is not solved herein. Therefore, the computational cost does not increase relative to simulations with the incompressible flow assumption.

**Fig. 18** presents the results of the temporal evolution of horizontal force on the rigid wall subjected to the high-aeration impact simulated with both the compressible and the incompressible solvers. First of all, it is clear to see that the peak impact is well-predicted with both solvers. Compared with the incompressible solver, an advantage of using the compressible solver is that the sub-atmospheric pressure (i.e., the trough after the peak) and the subsequent damped oscillations can be produced. However, the magnitude and the duration of the oscillation are much exaggerated. This is because in the physical experiment, the entrapped air pocket may not be completely wrapped by the vertical wall and the highly irregular free surface during the violent impact, resulting in a leakage of air from the pocket, which could

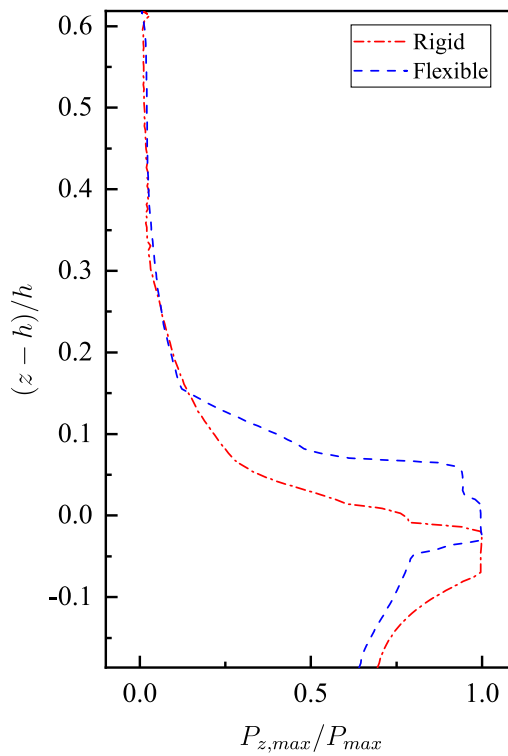


**Fig. 15.** Comparison of the spatial distribution of the peak pressure between the rigid and the flexible walls subjected to the *broken-wave* impact.

not be reproduced in the two-dimensional simulations. [Batlle Martin et al. \(2021\)](#) also found the significant pressure oscillations in the two-dimensional simulations were not observed in a three-dimensional configuration. Nevertheless, employing a three-dimensional configuration is computationally expensive for the present fully-coupled FSI simulation. Another problem is that the impact duration (both the rise time and fall time) is overestimated in the result predicted with the compressible solver, leading to an over-predicted impact impulse compared to the experimental result. This overestimation is also seen in Fig. 15 of [Ma et al. \(2016\)](#), who compared the results of the horizontal force obtained by *interFoam* and *compressibleInterFoam* for the plunging wave impact on a wall. When using the incompressible solver, the peak impact force and maximum quasi-hydrostatic force are in good agreement with the experimental measurement for the present cases, while the impact duration/impulse is under-predicted because the “bounce-back” is not considered ([Peregrine, 2003](#)). In addition, the sub-atmospheric pressure due to the air expansion is not able to be reproduced ([Zheng and Zhao, 2023](#)). Therefore, it seems neither the compressible nor incompressible solver can achieve 100% satisfactory for high-aeration impact at a large scale. Since the impact force is responsible for exciting high-order vibrations for structures, and the maximum quasi-hydrostatic force determines the peak structural displacement, using the assumption of incompressible fluid can provide sufficiently accurate input for the structural analysis. Although the subsequent damped oscillations after the peak impact force are not reproduced, the incompressible solver is consistent with the experimental measurement as the force oscillations rapidly become insignificant as shown in Fig. 18 from  $(t - t_0)/T = 0.24$  onward. Based on the facts discussed above, the incompressible solver is applied in the present study and is considered accurate enough for simulating relevant impact events when the sub-atmospheric pressure and the damped oscillations in the total force are not a focus for the problems studied.

## 6. Conclusions

Based on a fully-coupled CFD and CSM model, we have investigated the effect of hydroelasticity on four distinctive types of violent breaking wave impact at a large scale. The main conclusions are drawn as follows:

(1) Compared with the rigid wall, the profile of the peak pressure on the flexible wall subjected to violent breaking wave impacts shifts slightly upward. The structural deformation influences (not necessarily reduces) the impact force, impact duration, and impact impulse in progressive waves.

(2) The largest wave-induced wall displacement is reached under the maximum quasi-hydrostatic force, and its magnitude depends on the quasi-hydrostatic force amplitude. Excited by the impact, the flexible wall vibrates at a frequency very close to its natural frequency in vacuo, independent of the incident wave frequency.

(3) Subject to the peak impact force, high von Mises stress within the wall is observed near the impact region and at the toe of the wall. It is reduced in the flexible wall when compared to that in the rigid wall except for the *broken-wave* impact. Under the maximum quasi-hydrostatic force, the deformation of the flexible wall generally exacerbates the von Mises stress and wave overtopping. Consequently, the structural integrity of the rigid wall is more vulnerable to the peak impact force, whereas the structural integrity of the flexible wall is more susceptible to the maximum quasi-hydrostatic force.

(4) For the *high-aeration* impact at a large scale, our results suggest that the incompressible air assumption can provide reasonable predictions for the peak impact force and quasi-hydrostatic force but is less effective at reproducing the impact duration and sub-atmospheric pressure, compared with the compressible air assumption. However, the two-dimensional compressible simulation can lead to over-predicted pressure oscillations.

In summary, structural deformation significantly affects the characteristics of breaking wave impact and structural response in progressive waves. The findings in the present study contribute to further understanding of violent breaking wave impact on flexible structures, thereby supporting the design of existing and novel deformable offshore and coastal structures (e.g., the rubber/flexible membrane dams, storm surge gates/flood barriers, wave energy converters, etc.). In future studies, air compressibility, together with the effects of three-dimensionality and structural responses need to be considered for predictions of violent breaking wave impacts on structures at a large/full scale.

## CRediT authorship contribution statement

**Zhengyu Hu:** Conceptualization, Validation, Formal analysis, Investigation, Data curation, Visualization, Writing – original draft. **Yuzhu Li:** Conceptualization, Methodology, Resources, Writing – review & editing, Supervision, Project administration, Funding acquisition.

## Declaration of competing interest

The authors declare that they have no known competing financial interests or personal relationships that could have appeared to influence the work reported in this paper.

## Data availability

Data will be made available on request.

## Acknowledgments

This research is supported by the Ministry of Education, Singapore, under the Academic Research Fund Tier 1 (FY2021). This study is also supported in part with computational resources provided by the National Supercomputing Centre, Singapore (<https://www.nscc.sg>), under Project ID: 11002459.

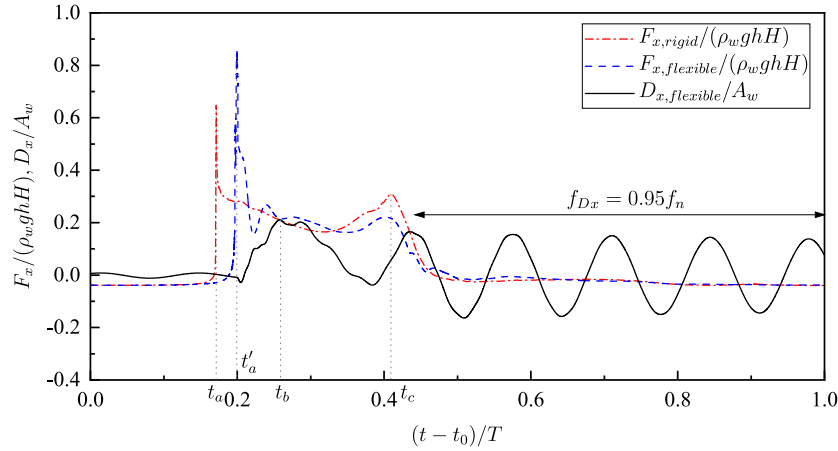


**Fig. 16.** Comparisons of the temporal evolution of horizontal force and the corresponding structural displacement between the rigid and the flexible walls subjected to the broken-wave impact.

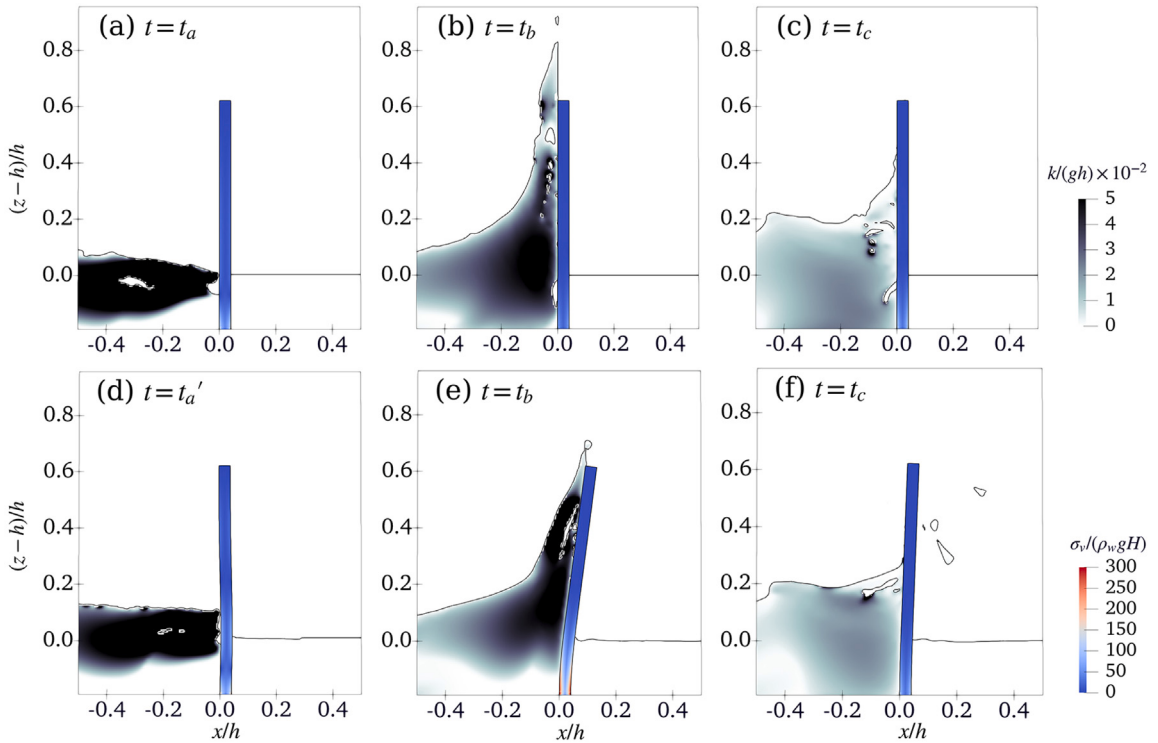


**Fig. 17.** Wave profiles, turbulence levels, and structural responses at typical time instants for the broken-wave impact. (a–c) Rigid wall. (d–e) Flexible wall.

## Appendix A. Fully-coupled CFD and CSM model

### A.1. Computational fluid dynamics

The flow in the Cartesian coordinate system is simulated by solving the Reynolds-averaged Navier–Stokes (RANS) equations:

$$\frac{\partial \bar{u}_i}{\partial x_i} = 0 \quad (A.1)$$

$$\frac{\partial \rho \bar{u}_i}{\partial t} + \bar{u}_j \frac{\partial \rho \bar{u}_i}{\partial x_j} = -\frac{\partial p^*}{\partial x_i} - g_j x_j \frac{\partial \rho}{\partial x_i} + \frac{\partial}{\partial x_j} (2\mu S_{ij} + \tau_{ij}) \quad (A.2)$$

where  $\bar{u}_i$  are the ensemble-averaged components of the velocity,  $x_i$  are the Cartesian coordinates,  $\rho$  is the density of the water-air mixture,  $p^*$  is the pressure in excess of hydrostatic,  $g_j$  is the gravitational acceleration,

$\mu = \rho v$  is the dynamic viscosity,  $v$  is the kinematic viscosity,  $t$  is the time,  $S_{ij}$  is the mean strain rate tensor given by

$$S_{ij} = \frac{1}{2} \left( \frac{\partial \bar{u}_i}{\partial x_j} + \frac{\partial \bar{u}_j}{\partial x_i} \right) \quad (A.3)$$

and  $\tau_{ij}$  is the Reynolds stress tensor given by the Boussinesq approximation

$$\tau_{ij} = -\overline{u'_i u'_j} = 2\nu_T S_{ij} - \frac{2}{3} k \delta_{ij} \quad (A.4)$$

where the overbar stands for Reynolds averaging and the prime denotes turbulent fluctuations,  $\nu_T$  is the eddy viscosity,  $\delta_{ij}$  is the Kronecker delta, and  $k$  is the turbulent kinetic energy per unit mass given by

$$k = \frac{1}{2} \overline{u'_i u'_i} \quad (A.5)$$

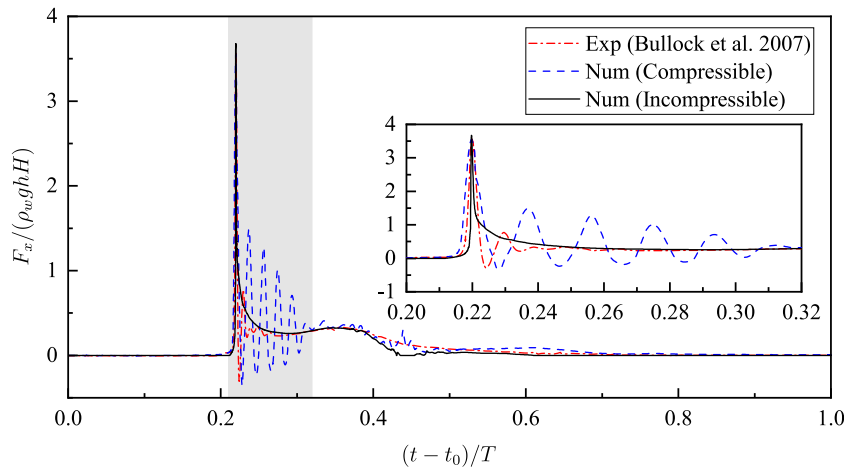


**Fig. 18.** Comparison of the temporal evolution of horizontal force on the rigid wall subjected to the *high-aeration* impact between the compressible and the incompressible flow assumptions.

Considering the wave breaking, the stabilized  $k - \omega$  turbulence model ( $\omega$  being the specific turbulent dissipation rate) of Larsen and Fuhrman (2018) is used to close the RANS equations. The turbulence model solves the transport equations for  $k$

$$\frac{\partial \rho k}{\partial t} + \bar{u}_j \frac{\partial \rho k}{\partial x_j} = \rho P_k - \rho P_b - \rho \beta^* k \omega + \frac{\partial}{\partial x_j} \left[ \left( \mu + \rho \sigma^* \frac{k}{\omega} \right) \frac{\partial k}{\partial x_j} \right] \quad (\text{A.6})$$

and the specific dissipation rate  $\omega$

$$\frac{\partial \rho \omega}{\partial t} + \bar{u}_j \frac{\partial \rho \omega}{\partial x_j} = \rho P_\omega - \rho \beta \omega^2 + \rho \frac{\sigma_d}{\omega} \frac{\partial k}{\partial x_j} \frac{\partial \omega}{\partial x_j} + \frac{\partial}{\partial x_j} \left[ \left( \mu + \rho \sigma \frac{k}{\omega} \right) \frac{\partial \omega}{\partial x_j} \right] \quad (\text{A.7})$$

The shear production for  $k$  is

$$P_k = \tau_{ij} \frac{\partial \bar{u}_i}{\partial x_j} = p_0 v_T, \quad p_0 = 2 S_{ij} S_{ij} \quad (\text{A.8})$$

and the buoyancy production for  $k$  is

$$P_b = -\frac{g_i}{\rho} \rho' \bar{u}'_i = p_b v_T, \quad p_b = \alpha_b^* N^2, \quad N^2 = \frac{g_i}{\rho} \frac{\partial \rho}{\partial x_i} \quad (\text{A.9})$$

where  $N$  is the Brunt-Vaisala frequency. The production of  $\omega$  is formulated as:

$$P_\omega = \alpha^* \frac{\omega}{k} \frac{\tilde{\omega}}{\tilde{\omega}} P_k = \alpha^* \frac{\omega}{\tilde{\omega}} p_0 \quad (\text{A.10})$$

In this model the eddy viscosity is defined as

$$v_T = \frac{k}{\tilde{\omega}} \quad (\text{A.11})$$

with

$$\tilde{\omega} = \max \left[ \tilde{\omega}, \lambda_2 \frac{\beta}{\beta^* \alpha^*} \frac{p_0}{p_\Omega} \omega \right], \quad \tilde{\omega} = \max \left[ \omega, \lambda_1 \sqrt{\frac{p_0 - p_b}{\beta^*}} \right] \quad (\text{A.12})$$

where

$$\rho_\Omega = 2 \Omega_{ij} \Omega_{ij}, \quad \Omega_{ij} = \frac{1}{2} \left( \frac{\partial \bar{u}_i}{\partial x_j} - \frac{\partial \bar{u}_j}{\partial x_i} \right) \quad (\text{A.13})$$

The standard closure coefficients utilized are directly taken from Wilcox (2006):  $\alpha^* = 0.52$ ,  $\beta = 0.0708$ ,  $\beta^* = 0.09$ ,  $\sigma = 0.5$ ,  $\sigma^* = 0.6$ ,  $\sigma_{do} = 0.125$ , with  $\sigma_d = H \left( \frac{\partial k}{\partial x_j} \frac{\partial \omega}{\partial x_j} \right) \sigma_{do}$ , where  $H(\cdot)$  is the Heaviside step function, which takes a value of unity if the argument is positive and zero otherwise.  $\alpha_b^* = 1.36$  and the stress limiting coefficients  $\lambda_1 = 0.2$  and  $\lambda_2 = 0.05$  following Larsen and Fuhrman (2018).

For the free surface simulation in the presence of waves, the Volume of Fluid (VOF) approach (Hirt and Nichols, 1981) is applied to represent the water-air interface. A phase indicator ( $\alpha$ ) is defined as the proportion of the water volume at each cell.  $\alpha$  varies from 0 to 1, where  $\alpha = 1$  indicates the cell is full of water and  $\alpha = 0$  denotes the

cell is full of air. The distribution of  $\alpha$  is governed by a liquid volume fraction transport equation:

$$\frac{\partial \alpha}{\partial t} + \frac{\partial \bar{u}_i \alpha}{\partial x_i} + \frac{\partial \bar{u}'_i \alpha (1 - \alpha)}{\partial x_i} = 0 \quad (\text{A.14})$$

where  $\bar{u}'_i$  is a relative velocity used to compress the interface. Any fluid property  $\Phi$  can be weighted in terms of  $\alpha$ :

$$\Phi = \alpha \Phi_{\text{water}} + (1 - \alpha) \Phi_{\text{air}} \quad (\text{A.15})$$

where water density  $\rho_w = 1000 \text{ kg/m}^3$ , air density  $\rho_a = 1 \text{ kg/m}^3$ , water dynamic viscosity  $\mu_w = 1 \times 10^{-3} \text{ N s/m}^2$ , and air dynamic viscosity  $\mu_a = 1.48 \times 10^{-5} \text{ N s/m}^2$ .

Considering the presence of the porous media (i.e., rubble-surfaced mound shown in Fig. 1) in the present study, the momentum equation (Eq. (A.2)) is reformulated as the volume-averaged RANS equations for the porous media (Jensen et al., 2014; Higuera et al., 2014):

$$(1 + C_m) \frac{\partial}{\partial t} \frac{\rho \bar{u}_i}{n} + \frac{\bar{u}_j}{n} \frac{\partial}{\partial x_j} \frac{\rho \bar{u}_i}{n} = - \frac{\partial p^*}{\partial x_i} - g_j x_j \frac{\partial \rho}{\partial x_i} + \frac{1}{n} \frac{\partial}{\partial x_j} (2 \mu S_{ij} + \tau_{ij}) - F_i \quad (\text{A.16})$$

where  $C_m = \gamma_p \frac{1-n}{n}$  is the added mass coefficient given by Van Gent (1995) and the empirical coefficient  $\gamma_p$  takes the value of 0.34,  $n$  is the porosity given as the ratio of the pore volume to the total volume, and  $F_i$  is the resistance force due to the presence of the porous region, which is expressed as (Van Gent, 1995):

$$F_i = \alpha_p \frac{(1-n)^2}{n^3} \frac{\mu}{d_{50}^2} \bar{u}_i + \beta_p \left( 1 + \frac{7.5}{KC} \right) \frac{1-n}{n^3} \frac{\rho}{d_{50}} \bar{u}_i |\bar{u}_i| \quad (\text{A.17})$$

where  $\alpha_p$  and  $\beta_p$  are empirical coefficients determined from experiments,  $d_{50}$  is the characteristic diameter of porous materials, and  $KC = u_m T / (nd_{50})$  is the Keulegan–Carpenter number, where  $u_m$  is the maximum wave orbital velocity and  $T$  is the wave period.

## A.2. Computational solid mechanics

The integration of momentum equation in the total Lagrangian form (refer to the initial undeformed configuration):

$$\int \rho_s \frac{\partial^2 D_i}{\partial t^2} dV = \oint \left( J W_{ij}^{-T} n_j \right) \sigma_{ik} dS + \int \rho_s g_j dV \quad (\text{A.18})$$

where  $\rho_s$  is the density of solid,  $D_i$  are the components of displacement,  $W_{ij}$  is the deformation gradient tensor given by  $W_{ij} = \delta_{ij} + \left( \frac{\partial D_i}{\partial x_j} \right)^T$ ,  $J$  is the Jacobian determinant of  $W_{ij}$ , and  $n_j$  are the components of

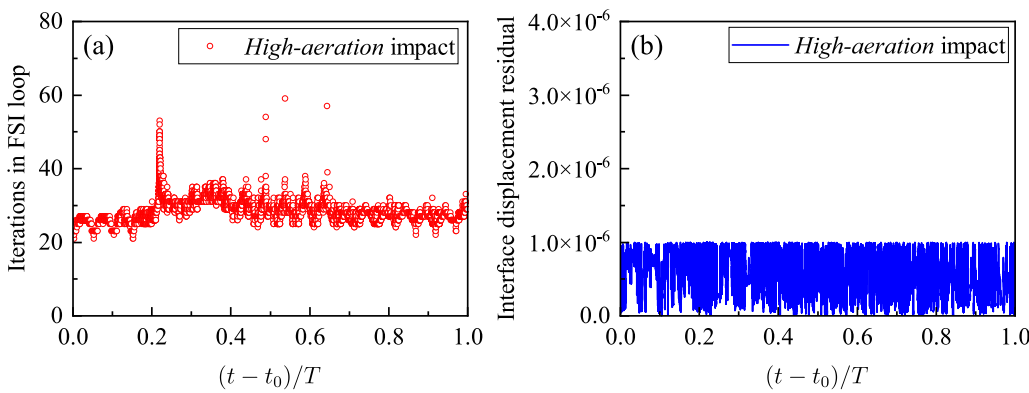


Fig. B.19. (a) Iterations and (b) fluid–solid interface displacement residual in the FSI loop.

the outward facing normal vector. The Cauchy stress tensor  $\sigma_{ij}$  can be obtained by the displacement vector:

$$\sigma_{ij} = G \operatorname{dev}[J^{-2/3} W_{ki} W_{kj}] + \frac{\kappa}{2} \left( \frac{J^2 - 1}{J} \right) \delta_{ij} \quad (\text{A.19})$$

where  $G$  and  $\kappa$  are the shear modulus and bulk modulus, given by:

$$G = \frac{E}{2(1+\nu)} \quad (\text{A.20})$$

$$\kappa = \frac{E}{3(1-2\nu)} \quad (\text{A.21})$$

where  $E$  and  $\nu$  are Young's modulus and Poisson's ratio, respectively.

### A.3. Fully-coupled scheme

A fully-coupled scheme implemented by Tuković et al. (2018) is employed for the solutions involving the fluid and solid domains based on a partitioned scheme. At every time step, the fluid and solid domains are solved alternately and iteratively. The momentum and kinematic continuities at the fluid–solid interface are achieved by a Dirichlet–Neumann approach. Specifically, the pressure and velocity fields are first acquired from the fluid domain. Then the fluid force is passed onto the solid interface to satisfy the dynamic condition:

$$n_i \sigma_{ij,\text{fluid}} = n_i \sigma_{ij,\text{solid}} \quad (\text{A.22})$$

where  $\sigma_{ij,\text{fluid}}$  is the stress in the fluid domain. The solution of the solid domain is obtained with this Neumann condition (traction) at the interface boundary. The velocity of the solid interface then passes back to the fluid interface using the Aitken under-relaxation approach, i.e., the relaxation factor varies in the FSI coupling to quickly reduce the displacement residual. The fluid domain is therefore solved with a Dirichlet condition of velocity at the interface to satisfy the kinematic condition:

$$u_{i,\text{fluid}} = u_{i,\text{solid}} \quad (\text{A.23})$$

The mesh of the fluid domain is updated at the end of the FSI iteration. Some iterations are required for each time step to achieve a continuous displacement across the interface:

$$D_{i,\text{fluid}} = D_{i,\text{solid}} \quad (\text{A.24})$$

## Appendix B. Convergence of FSI iterations

See Fig. B.19.

## References

- Attili, T., Heller, V., Triantafyllou, S., 2023. Wave impact on rigid and flexible plates. *Coast. Eng.* 104302. <http://dx.doi.org/10.1016/j.coastaleng.2023.104302>.
- Babarit, A., 2017. *Ocean Wave Energy Conversion: Resource, Technologies and Performance*. Elsevier.
- Bagnold, R.A., 1939. Interim report on wave-pressure research. *J. Inst. Civ. Eng.* 12 (7), 202–226. <http://dx.doi.org/10.1680/ijoti.1939.14539>.
- Battle Martin, M., Pinon, G., Reveillon, J., Kimmoun, O., 2021. Computations of soliton impact onto a vertical wall: Comparing incompressible and compressible assumption with experimental validation. *Coast. Eng.* 164, 103817. <http://dx.doi.org/10.1016/j.coastaleng.2020.103817>.
- Bredmose, H., Bullock, G.N., Hogg, A.J., 2015. Violent breaking wave impacts. Part 3: Effects of scale and aeration. *J. Fluid Mech.* 765, 82–113. <http://dx.doi.org/10.1017/jfm.2014.692>.
- Bredmose, H., Peregrine, D.H., Bullock, G.N., 2009. Violent breaking wave impacts. Part 2: modelling the effect of air. *J. Fluid Mech.* 641, 389–430. <http://dx.doi.org/10.1017/S0022112009991571>.
- Brown, S.A., Greaves, D.M., Magar, V., Conley, D.C., 2016. Evaluation of turbulence closure models under spilling and plunging breakers in the surf zone. *Coast. Eng.* 114, 177–193. <http://dx.doi.org/10.1016/j.coastaleng.2016.04.002>.
- Bullock, G.N., Obhrai, C., Peregrine, D.H., Bredmose, H., 2007. Violent breaking wave impacts. Part 1: Results from large-scale regular wave tests on vertical and sloping walls. *Coast. Eng.* 54 (8), 602–617. <http://dx.doi.org/10.1016/j.coastaleng.2006.12.002>.
- Cardiff, P., Karač, A., De Jaeger, P., Jasak, H., Nagy, J., Ivanković, A., Tuković, Ž., 2018. An open-source finite volume toolbox for solid mechanics and fluid–solid interaction simulations. arXiv preprint [arXiv:1808.10736](https://arxiv.org/abs/1808.10736).
- Chanson, H., 1997. A review of the overflow of inflatable flexible membrane dams. *Aust. Civ. Eng. Trans.* 39 (2/3), 107–116.
- Collins, I., Hossain, M., Dettmer, W., Masters, I., 2021. Flexible membrane structures for wave energy harvesting: A review of the developments, materials and computational modelling approaches. *Renew. Sustain. Energy Rev.* 151, 111478. <http://dx.doi.org/10.1016/j.rser.2021.111478>.
- Cooker, M.J., Peregrine, D.H., 1990. Violent water motion at breaking-wave impact. In: *Proceedings of the 22nd International Conference on Coastal Engineering*. pp. 164–176.
- Devolder, B., Troch, P., Rauwoens, P., 2018. Performance of a buoyancy-modified  $k-\omega$  and  $k-\omega$  SST turbulence model for simulating wave breaking under regular waves using OpenFOAM®. *Coast. Eng.* 138, 49–65. <http://dx.doi.org/10.1016/j.coastaleng.2018.04.011>.
- Diamantoulaki, I., Angelides, D.C., Manolis, G.D., 2008. Performance of pile-restrained flexible floating breakwaters. *Appl. Ocean Res.* 30 (4), 243–255. <http://dx.doi.org/10.1016/j.apor.2009.03.004>.
- Fenton, J.D., 1988. The numerical solution of steady water wave problems. *Comput. Geosci.* 14 (3), 357–368. [http://dx.doi.org/10.1016/0098-3004\(88\)90066-0](http://dx.doi.org/10.1016/0098-3004(88)90066-0).
- Fuhrman, D.R., Li, Y., 2020. Instability of the realizable  $k-\epsilon$  turbulence model beneath surface waves. *Phys. Fluids* 32 (11), 115108. <http://dx.doi.org/10.1063/5.0029206>.
- Hattori, M., Tsujioka, N., 1996. Dynamic response of vertical elastic walls to breaking wave impact. In: *Coastal Engineering 1996*. pp. 2456–2469. <http://dx.doi.org/10.1061/9780784402429.190>.
- Higuera, P., Lara, J.L., Losada, I.J., 2013. Realistic wave generation and active wave absorption for Navier–Stokes models: Application to OpenFOAM®. *Coast. Eng.* 71, 102–118. <http://dx.doi.org/10.1016/j.coastaleng.2012.07.002>.
- Higuera, P., Lara, J.L., Losada, I.J., 2014. Three-dimensional interaction of waves and porous coastal structures using OpenFOAM®. Part I: Formulation and validation. *Coast. Eng.* 83, 243–258. <http://dx.doi.org/10.1016/j.coastaleng.2013.08.010>.

- Hirt, C.W., Nichols, B.D., 1981. Volume of fluid (VOF) method for the dynamics of free boundaries. *J. Comput. Phys.* 39 (1), 201–225. [http://dx.doi.org/10.1016/0021-9991\(81\)90145-5](http://dx.doi.org/10.1016/0021-9991(81)90145-5).
- Hu, Z., Huang, L., Li, Y., 2023. Fully-coupled hydroelastic modeling of a deformable wall in waves. *Coast. Eng.* 179, 104245. <http://dx.doi.org/10.1016/j.coastaleng.2022.104245>.
- Huang, L., Li, Y., 2022. Design of the submerged horizontal plate breakwater using a fully coupled hydroelastic approach. *Comput.-Aided Civ. Infrastruct. Eng.* 37 (7), 915–932. <http://dx.doi.org/10.1111/mice.12784>.
- Huang, L., Ren, K., Li, M., Tuković, Ž., Cardiff, P., Thomas, G., 2019. Fluid-structure interaction of a large ice sheet in waves. *Ocean Eng.* 182, 102–111. <http://dx.doi.org/10.1016/j.oceaneng.2019.04.015>.
- Issa, R.I., 1986. Solution of the implicitly discretised fluid flow equations by operator-splitting. *J. Comput. Phys.* 62 (1), 40–65. [http://dx.doi.org/10.1016/0021-9991\(86\)90099-9](http://dx.doi.org/10.1016/0021-9991(86)90099-9).
- Jensen, B., Jacobsen, N.G., Christensen, E.D., 2014. Investigations on the porous media equations and resistance coefficients for coastal structures. *Coast. Eng.* 84, 56–72. <http://dx.doi.org/10.1016/j.coastaleng.2013.11.004>.
- Kimmoun, O., Malenica, S., Scolan, Y., 2009. Fluid structure interactions occurring at a flexible vertical wall impacted by a breaking wave. In: *The Nineteenth International Offshore and Polar Engineering Conference, Vol. 3. ISOPE-I-09-035*, pp. 308–315.
- Kirkgoz, M.S., 1995. Breaking wave impact on vertical and sloping coastal structures. *Ocean Eng.* 22 (1), 35–48. [http://dx.doi.org/10.1016/0029-8018\(93\)E0006-E](http://dx.doi.org/10.1016/0029-8018(93)E0006-E).
- Kirkgoz, M.S., Aköz, M.S., 2005. Geometrical properties of perfect breaking waves on composite breakwaters. *Ocean Eng.* 32 (16), 1994–2006. <http://dx.doi.org/10.1016/j.oceaneng.2005.01.003>.
- Kumar, G.M., Sriram, V., 2020. Development of a hybrid model based on mesh and meshfree methods and its application to fluid-elastic structure interaction for free surface waves. *J. Fluids Struct.* 99, <http://dx.doi.org/10.1016/j.jfluidstructs.2020.103159>.
- Larsen, B.E., Fuhrman, D.R., 2018. On the over-production of turbulence beneath surface waves in Reynolds-averaged Navier-Stokes models. *J. Fluid Mech.* 853, 419–460. <http://dx.doi.org/10.1017/jfm.2018.577>.
- Launder, B.E., Reece, G.J., Rodi, W., 1975. Progress in the development of a Reynolds-stress turbulence closure. *J. Fluid Mech.* 68 (3), 537–566. <http://dx.doi.org/10.1017/S0022112075001814>.
- Li, Y., Fuhrman, D.R., 2021. Computational fluid dynamics simulation of deep-water wave instabilities involving wave breaking. *J. Offshore Mech. Arct. Eng.* 144 (2), <http://dx.doi.org/10.1115/1.4052277>.
- Li, Y., Fuhrman, D.R., 2022. On the turbulence modelling of waves breaking on a vertical pile. *J. Fluid Mech.* 953, A3. <http://dx.doi.org/10.1017/jfm.2022.941>.
- Li, Y., Larsen, B.E., Fuhrman, D.R., 2022. Reynolds stress turbulence modelling of surf zone breaking waves. *J. Fluid Mech.* 937, A7. <http://dx.doi.org/10.1017/jfm.2022.92>.
- Liao, K., Hu, C., 2013. A coupled FDM-FEM method for free surface flow interaction with thin elastic plate. *J. Mar. Sci. Technol.* 18 (1), 1–11. <http://dx.doi.org/10.1007/s00773-012-0191-0>.
- Liao, K., Hu, C., Sueyoshi, M., 2015. Free surface flow impacting on an elastic structure: Experiment versus numerical simulation. *Appl. Ocean Res.* 50, 192–208. <http://dx.doi.org/10.1016/j.apor.2015.02.002>.
- Lin, P., Liu, P.L.F., 1998. A numerical study of breaking waves in the surf zone. *J. Fluid Mech.* 359, 239–264. <http://dx.doi.org/10.1017/S002211209700846X>.
- Liu, S., Gatin, I., Obhrai, C., Ong, M.C., Jasak, H., 2019. CFD simulations of violent breaking wave impacts on vertical wall using a two-phase compressible solver. *Coast. Eng.* 154, 103564. <http://dx.doi.org/10.1016/j.coastaleng.2019.103564>.
- Lugni, C., Broccolini, M., Faltinsen, O.M., 2006. Wave impact loads: The role of the flip-through. *Phys. Fluids* 18 (12), 122101. <http://dx.doi.org/10.1063/1.2399077>.
- Ma, Z.H., Causon, D.M., Qian, L., Mingham, C.G., Martínez Ferrer, P., 2016. Numerical investigation of air enclosed wave impacts in a depressurised tank. *Ocean Eng.* 123, 15–27. <http://dx.doi.org/10.1016/j.oceaneng.2016.06.044>.
- Melville, W.K., 1982. The instability and breaking of deep-water waves. *J. Fluid Mech.* 115, 165–185. <http://dx.doi.org/10.1017/S0022112082000706>.
- Michailides, C., Angelides, D.C., 2012. Modeling of energy extraction and behavior of a flexible floating breakwater. *Appl. Ocean Res.* 35, 77–94. <http://dx.doi.org/10.1016/j.apor.2011.11.004>.
- Murawski, L., 2005. Shaft line alignment analysis taking ship construction flexibility and deformations into consideration. *Mar. Struct.* 18 (1), 62–84. <http://dx.doi.org/10.1016/j.marstruc.2005.05.002>.
- Oumeraci, H., 1994. Review and analysis of vertical breakwater failures — lessons learned. *Coast. Eng.* 22 (1), 3–29. [http://dx.doi.org/10.1016/0378-3839\(94\)90046-9](http://dx.doi.org/10.1016/0378-3839(94)90046-9).
- Oumeraci, H., Kortenhaus, A., Allsop, W., de Groot, M., Crouch, R., Vrijling, H., Voortman, H., 2001. Probabilistic Design Tools for Vertical Breakwaters. CRC Press.
- Peregrine, D.H., 2003. Water-wave impact on walls. *Annu. Rev. Fluid Mech.* 35 (1), 23–43. <http://dx.doi.org/10.1146/annurev.fluid.35.101101.161153>.
- Peregrine, D., Bredmose, H., Bullock, G., Obrhai, C., Müller, G., Wolters, G., 2005. Water wave impact on walls and the role of air. In: Proc. 29th Int. Conf. Coastal Engineering 2004, Vol. 4. World Scientific, pp. 4005–4017. [http://dx.doi.org/10.1142/9789812701916\\_0323](http://dx.doi.org/10.1142/9789812701916_0323).
- Raby, A., Bullock, G., Jonathan, P., Randell, D., Whittaker, C., 2022. On wave impact pressure variability. *Coast. Eng.* 177, 104168. <http://dx.doi.org/10.1016/j.coastaleng.2022.104168>.
- Rane, A.V., Thakur, S., Thakur, R., 2019. 1 - Rubber Dam—An Introduction. In: *Hydraulic Rubber Dam*, William Andrew Publishing, pp. 1–9. <http://dx.doi.org/10.1016/B978-0-12-812210-5.00001-8>.
- Ravindar, R., Sriram, V., 2021. Impact pressure and forces on a vertical wall with different types of parapet. *J. Waterw. Port Coast. Ocean Eng.* 147 (3), 04021007. [http://dx.doi.org/10.1061/\(ASCE\)WW.1943-5460.0000635](http://dx.doi.org/10.1061/(ASCE)WW.1943-5460.0000635).
- Ravindar, R., Sriram, V., Schimmels, S., Stagonas, D., 2019. Characterization of breaking wave impact on vertical wall with recurve. *ISH J. Hydraul. Eng.* 25 (2), 153–161. <http://dx.doi.org/10.1080/09715010.2017.1391132>.
- Ravindar, R., Sriram, V., Schimmels, S., Stagonas, D., 2022. Laboratory study on breaking wave impact on a vertical wall with recurved parapets in small and large scale. In: *The 32nd International Ocean and Polar Engineering Conference, Vol. All Days. ISOPE-I-22-245*.
- Sriram, V., Ma, Q.W., 2012. Improved MLPG\_R method for simulating 2D interaction between violent waves and elastic structures. *J. Comput. Phys.* 231 (22), 7650–7670. <http://dx.doi.org/10.1016/j.jcp.2012.07.003>.
- Tanimoto, K., Takahashi, S., 1994. Design and construction of caisson breakwaters — the Japanese experience. *Coast. Eng.* 22 (1), 57–77. [http://dx.doi.org/10.1016/0378-3839\(94\)90048-5](http://dx.doi.org/10.1016/0378-3839(94)90048-5).
- Tieleman, O.C., Tsouvalas, A., Hofland, B., Peng, Y., Jonkman, S.N., 2019. A three dimensional semi-analytical model for the prediction of gate vibrations immersed in fluid. *Mar. Struct.* 65, 134–153. <http://dx.doi.org/10.1016/j.marstruc.2018.12.007>.
- Tuković, Ž., Karač, A., Cardiff, P., Jasak, H., Ivanković, A., 2018. OpenFOAM finite volume solver for fluid-solid interaction. *Trans. FAMENA* 42 (3), 1–31. <http://dx.doi.org/10.21278/TOF.42301>.
- Van Gent, M.R.A., 1995. *Wave Interaction with Permeable Coastal Structures (Ph.D. thesis)*. Delft University.
- Wang, H., Zhu, X., Cheng, Y.S., Liu, J., 2014. Experimental and numerical investigation of ship structure subjected to close-in underwater shock wave and following gas bubble pulse. *Mar. Struct.* 39, 90–117. <http://dx.doi.org/10.1016/j.marstruc.2014.07.003>.
- Wilcox, D.C., 2006. *Turbulence Modeling for CFD, third ed.* DCW Industries.
- Zheng, K., Zhao, X., 2023. Impact of multiphase flow simulation of breaking waves on a vertical seawall with a recurved parapet. *Int. J. Offshore Polar Eng.* 33 (02), 141–147. <http://dx.doi.org/10.17736/ijope.2023.ak54>.